ChemSusChem

Review
doi.org/10.1002/cssc.202400898

Chemistry Europe
European Chemical Societies Publishing

www.chemsuschem.org

Multiscale Modeling of CO_2 Electrochemical Reduction on Copper Electrocatalysts: A Review of Advancements, Challenges, and Future Directions

Reza Gholizadeh,*[a] Matic Pavlin,[a] Matej Huš,*[a, b, c, d] and Blaž Likozar*[a]

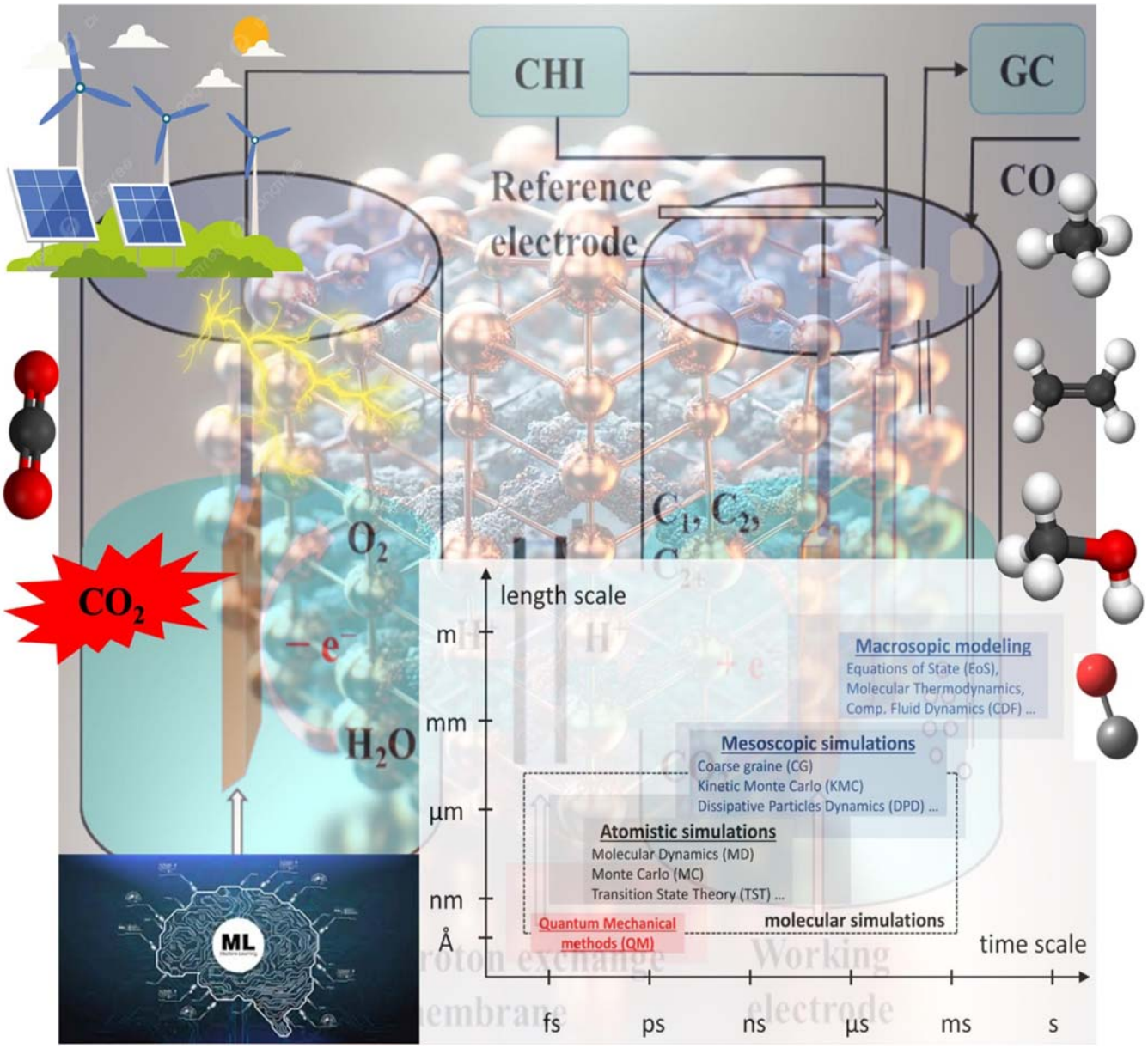

Although CO_2 contributes significantly to global warming, it also offers potential as a raw material for the production of hydrocarbons such as CH_4, C_2H_4 and CH_3OH. Electrochemical CO_2 reduction reaction (eCO_2RR) is an emerging technology that utilizes renewable energy to convert CO_2 into valuable fuels, solving environmental and energy problems simultaneously. Insights gained at any individual scale can only provide a limited view of that specific scale. Multiscale modeling, which involves coupling atomistic-level insights (density functional theory, DFT) and (Molecular Dynamics, MD), with mesoscale (kinetic Monte Carlo, KMC, and microkinetics, MK) and macroscale (computational fluid dynamics, CFD) simulations, has received significant attention recently. While multiscale modeling of eCO_2RR on electrocatalysts across all scales is limited due to its complexity, this review offers an overview of recent works on single scales and the coupling of two and three scales, such as "DFT + MD", "DFT + KMC", "DFT + MK", "KMC/MK + CFD" and "DFT + MK/KMC + CFD", focusing particularly on Cu-based electrocatalysts as copper is known to be an excellent electrocatalyst for eCO_2RR. This sets it apart from other reviews that solely focus exclusively on a single scale or only on a combination of DFT and MK/KMC scales. Furthermore, this review offers a concise overview of machine learning (ML) applications for eCO_2RR, an emerging approach that has not yet been reviewed. Finally, this review highlights the key challenges, research gaps and perspectives of multiscale modeling for eCO_2RR.

1. Introduction

Global CO_2 emissions from fossil fuels and cement increased by 1.1% in 2023 compared to 2022, reaching a new record high of 36.8 billion tons (Figure 1). This growth is 1.4% above pre-COVID-19 level (2019), according to the Global Carbon Budget report by the Global Carbon Project.[1] The concentration of CO_2 in the atmosphere has risen continuously from 315 ppm in 1959 to 422 ppm in 2023.[2] The World Meteorological Organization (WMO) has confirmed that 2023 was the warmest year on record, with the annual average global temperature of 1.45 ± 0.12 °C above pre-industrial levels.[3] Converting CO_2 into other useful materials by creating a sustainable recycling system is one of the solutions to the decreasing climate risks.[4,5] Due to its remarkable inertness, the conversion of CO_2 can only occur under extreme reaction conditions, which include high pressure, high temperatures and high overvoltages.[6] To date, several processes have been used to convert CO_2 into C-based materials, such as chemical reforming,[7,8] biological,[9] mineralization,[10] photochemical,[11,12] and electrochemical methods.[13] The sequential chemical reactions that occur in CO_2 reduction are known as either CO_2RR or CO_2 hydrogenation.[14]

The aqueous electrochemical reduction of CO_2 (eCO_2RR) proceeds under mild conditions (20–25 °C) and ambient pressure (1 atm), using water as an abundant, readily available and inexpensive source.[15] Computational and experimental investigations reveal that eCO_2RR and eCORR have the same sequence and product distribution, since CO_2 is also converted to CO, which is a crucial intermediate for the generation of C_2^+ products by coupling of C atoms.[16–18] The electrocatalyst materials, cell structure, electrolyte pH and operating potential affect the catalyst efficiency and selectivity of the eCO_2RR.[19] The reaction takes place on the surface of the electrocatalyst, which serves as the cathode of an electrochemical cell, and the productivity of the reaction depends on the catalytic activity of the electrocatalyst.[20,21]

The metal catalysts are classified based on the binding energies of the key species (CO*, H*, OCHO*, and COOH*).[22] The catalysts can be classified into four categories: (*i*) Cd, Sn, Tl, Bi, Hg and Pb have the highest performance in the production of $HCOO^-$,[23,24] (*ii*) Ga, Ag, Zn, Au and Pd are most suitable for the production of CO,[25–27] (*iii*) while Ni, Fe, Pt, and Ti are suitable for the reduction of H_2O to H_2 instead of CO_2. Finally, (*iv*) copper (Cu) is a clearly superior catalyst for the production of a wide range of chemicals.[28,29] Thus, Cu is the only known high-performance metal electrocatalyst that can transfer two electrons to hydrocarbons and fuels in eCO_2RR. Due to the multi-electron reduction reactions, products such as ethylene and propane have greater energy storage capacity and are more valuable than HCOOH and CO.[30] Table 1 shows the

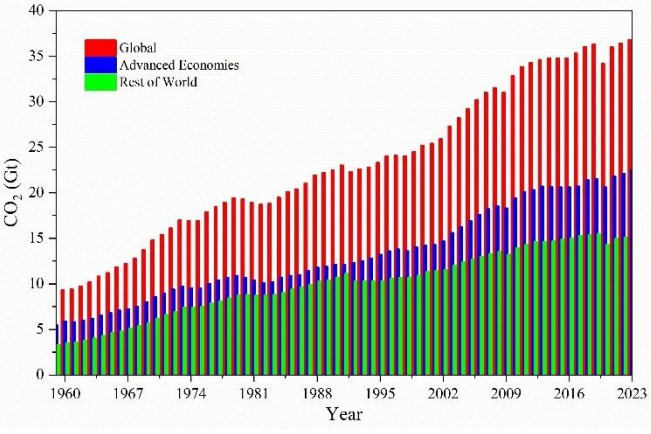

Figure 1. Energy-related CO_2 emissions from 1959 to 2023 (Global in Red, Advanced Economies in Blue and Rest of World in Green).

[a] *Department of Catalysis and Chemical Reaction Engineering, National Institute of Chemistry, Ljubljana, Slovenia*
[b] *Association for Technical Culture of Slovenia, Ljubljana, Slovenia*
[c] *Institute for the Protection of Cultural Heritage of Slovenia, Conservation Centre, Research Institute, Ljubljana, Slovenia*
[d] *University of Nova Gorica, Nova Gorica, Ljubljana, Slovenia*

Correspondence: *Reza Gholizadeh, Matej Huš and Blaž Likozar, Department of Catalysis and Chemical Reaction Engineering, National Institute of Chemistry, Hajdrihova 19, Ljubljana SI-1000, Slovenia. Email: reza.gholizadeh@ki.si and matej.hus@ki.si and blaz.likozar@ki.si*

Table 1. Performances (%) of eCO_2RR for generation of different products onto a variety of catalysts at T = 18.5 °C, pH = 6.8.[31]

Catalyst	J_{total} [mA/cm^2]	E [V vs RHE]	Methane	Ethylene	Ethanol	Propanol	Carbon Monoxide	Formate	Hydrogen	Total
Pb	−5.0	−1.24	0	0	0	0	0	97.4	5.0	102.4
Hg	−0.5	−1.12	0	0	0	0	0	99.5	0	99.5
Tl	−5.0	−1.21	0	0	0	0	0	95.1	6.2	101.3
In	−5.0	−1.16	0	0	0	0	2.1	94.9	3.3	100.3
Sn	−5.0	−1.09	0	0	0	0	7.1	88.4	4.6	100.1
Cd	−5.0	−1.24	1.3	0	0	0	13.9	78.4	9.4	103.0
Au	−5.0	−0.65	0	0	0	0	87.1	0.7	10.2	98.0
Ag	−5.0	−0.98	0	0	0	0	81.5	0.6	12.4	94.6
Zn	−5.0	−1.15	0	0	0	0	79.4	6.1	9.9	95.4
Pd	−5.0	−0.81	2.9	0	0	0	28.3	2.8	26.2	60.2
Ga	−5.0	−0.85	0	0	0	0	23.2	0	79.0	102.0
Cu	−5.0	−1.05	33.3	25.5	5.7	3.0	1.3	9.4	20.5	103.5
Ni	−5.0	−1.09	1.8	0.1	0	0	0	1.4	88.9	92.4
Fe	−5.0	−0.52	0	0	0	0	0	0	94.8	94.8
Pt	−5.0	−0.68	0	0	0	0	0	0.1	95.7	95.8
Ti	−5.0	−1.21	0	0	0	0	0	0	99.7	99.7

efficiency of various catalysts in CO_2RR.[31] The rest of this review will focus on Cu-based catalysts. We provide an overview of theoretical advances in multiscale modeling, highlighting the coupling of different scales and recent developments in catalysts over the last decade in the field of eCO_2RR (see Figure 2a and b).

This review focuses on multiscale modeling in the field of eCO_2RR, as the coupling of different scales offers unique insights by combining the fundamental molecular-scale mechanisms (DFT and MD scales) with the mesoscale kinetics (KMC scale) and the macroscale reactor performance (CFD scale). Here we present the latest advances in modeling different scales and in particular their coupling. A comprehensive multi-

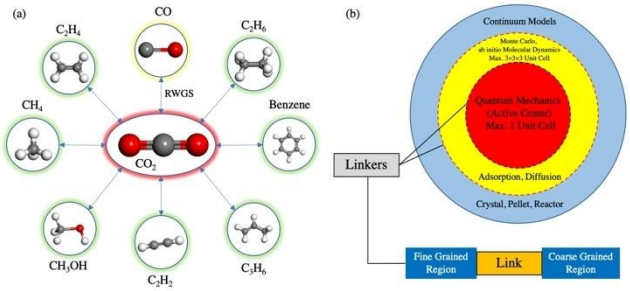

Figure 2. An overview of the scope of the review, (a) CO_2 electrochemical reduction to hydrocarbons (b) Multiscale modeling.

Professor Blaž Likozar is the head of the Department of Catalysis and Chemical Reaction Engineering at the National Institute of Chemistry (Ljubljana, Slovenia). He leads numerous research projects, including 15 in H2020/30 in Horizon Europe, and is involved in several industrial projects. His areas of expertise include heterogeneous catalysis, chemical kinetics and modeling.

Dr. Matej Huš is a senior researcher at the National Institute of Chemistry (Ljubljana, Slovenia) and a lecturer at the University of Nova Gorica. His field of expertise is computational chemistry, with an emphasis on nitrogen fixation, carbon dioxide hydrogenation, methane activation, ethylene epoxidation, and biomass valorization.

Dr. Reza Gholizadeh is a senior researcher at the National Institute of Chemistry (Ljubljana, Slovenia). His research topics include electrocatalysis, electrochemical energy conversion, and CO_2 reduction. He has experience in heterogeneous catalysis, DFT calculations, kinetics and thermodynamics.

Dr. Matic Pavlin obtained his PhD at RWTH Aachen University followed by PostDoc positions at CNR-IOM Trieste-SISSA and University of Ljubljana. He is currently a Research Associate in the Department of Catalysis and Chemical Reaction Engineering at the National Institute of Chemistry (Ljubljana, Slovenia). His research focuses mainly on MD Simulations and free energy calculations of chemical reactions, including heterogenous catalysis and non-catalysed reactions.

scale model has the potential to identify selective reduction mechanisms, improve catalyst design and optimize the overall efficiency of the eCO_2RR process. This approach enables the optimization of eCO_2RR catalysts and reactors within a unified framework based on fundamental principles, moving away from empirical trial-and-error methods. By more accurately representing the intricate interactions involved in eCO_2RR, a comprehensive model covering all scales enables accurate predictions and optimizations in catalyst development and reaction conditions.

The value of such a model lies in its ability to provide a holistic perspective of the eCO_2RR process, facilitating the development of more efficient and selective catalysts and thus advancing the field of sustainable and environmentally friendly energy solutions.

Theoretical and experimental experts working in the field of CO_2RR, especially with copper electrocatalysts, can benefit from this review. It provides an understanding of the phenomena that occur during the reaction at different scales and the role of Cu-based electrocatalysts in eCO_2RR. This review differs from others that solely focus exclusively on a single scale or a combination of DFT and MK/KMC scales, as it collects rare studies that have investigated coupling across all scales in eCO_2RR. In addition, this paper explores the application of machine learning and artificial intelligence in this area, an area that has not been extensively covered in previous reviews. This comprehensive and insightful review offers a unique perspective on the topic, providing valuable insights and potential future research directions not covered elsewhere.

1.1. Fundamentals and Reaction Mechanisms of eCO_2RR

1.1.1. Fundamentals

The efficiency of eCO_2RR depends on the longevity and selectivity of the anode (oxygen evolution reaction, OER) and the cathode (CO_2RR). In addition, a high conductivity of the electrodes and electrolytes, which enables a higher mass transport of the species through the electrocatalyst layers, plays a significant role for a higher efficiency of the eCO_2RR. The following parameters describe or influence the efficiency[32]:

a) Faradaic efficiency (FE) is the fraction of electrons used to form a given product and is directly related to the selectivity of the catalyst. In theoretical modeling, it is useful to express FE in terms of changes in Gibbs free energy, which can be obtained directly from DFT calculations. FE for a given product in a multiproduct electrochemical reaction can be defined as follows:

$$\varepsilon_{Faradaic} = \frac{Q_n}{Q_{total}} = \frac{\alpha n F}{Q_{total}} \quad (1)$$

where Q_n, Q_{total}, α, n and F are the charge for the production of a given product, the total charge transferred by the electrochemical cell, the number of electrons released in the electrochemical reaction (α is equal to 2 & 8 for eCO_2RR to CO and CH_4), the number of moles for the product of interest and the Faraday constant, respectively. The FE depends on the composition and structure of the catalysts.[33]

b) Energetic efficiency (EE) measures the amount of energy consumed for a particular product and is computed as follows:

$$\varepsilon_{energetic} = \frac{E_{eq}}{E_{eq} + \eta} \times \varepsilon_{Faradaic} \quad (2)$$

where E_{eq} and η denote the equilibrium potential and the overpotential, respectively. High energy efficiency is achieved with low overpotentials and high FE.

c) Current density (j) normalizes the current through the surface of the working electrode (WE) and indicates the dimension of the electrolyzer. The partial current density of a particular product (j_n) is obtained from the FE and the current density:

$$j_n = j \times FE \quad (3)$$

d) Tafel plot which is based on the Butler-Volmer relationship, establishes a link between current density and overpotential and provides an insight into the reaction mechanisms and the efficiency of the electrocatalyst.

A lower Tafel slope means higher catalytic efficiency. In eCO2RR, the initial one-electron transfer step is the rate-determining step (118 mV/dec), while the slope of 59 mV/dec indicates a pre-equilibrium step that precedes the subsequent rate-limiting chemical process.[45,46] Other parameters that define the efficiency of CO_2RR and evaluate its economic feasibility are electrocatalyst stability, current density, and costs.[47]

1.1.2. Reaction Mechanisms

eCO_2RR leads to a variety of products via different reaction pathways. It is a complex reaction as several electrons and protons are transferred during the conversion.[48,49] As shown in Figure 3a, the conversion of the linear CO_2 molecule to the bent radical CO_2^- is the first step of CO_2RR. The generated CO_2^- radicals are then converted to formate (OCHO*) or *cis*-, *trans*-COOH* by H^+ adsorption. Later, the OCHO* intermediate is converted to HCOOH, while COOH* is converted to CO*, which is an important intermediate[50,51] as selectivity depends on its adsorption energy.[52] The generated CO* can be converted to CHO* (formyl) and COH* (hydroxy-methylidyne), which[53–55] upon further reduction are converted to CH_3OH and CH_4 molecules. Another important role of CO* is the conversion to C_2^+ molecules by CO* dimerization.[56,57] Figure 3a shows several plausible mechanistic reaction routes over Cu-based electrocatalysts.

1.1.3. Products of eCO_2RR

During the eCO_2RR process, different products can be generated, which are classified as C_1, C_2, C_3 and C_4^+. Since HER also

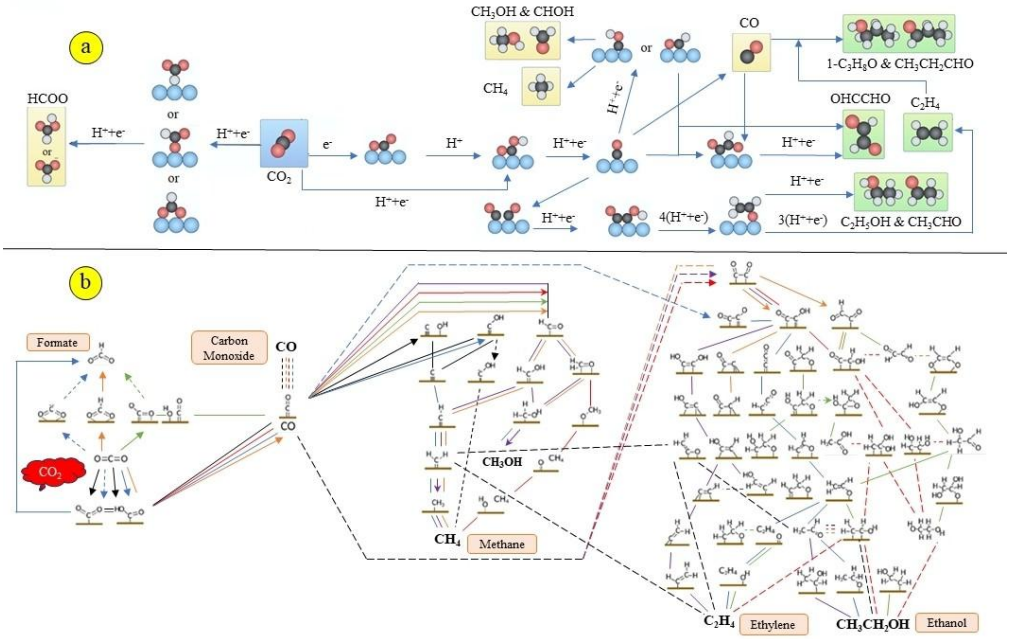

Figure 3. (a) Based on the studies in the legend, plausible reaction mechanisms for the eCO_2RR to C1 and C2 chemicals over Cu-based electrocatalysts are categorized in various colored reaction schemes: (a) Chen et al.,[34] Reprinted with permission from refs,[34,35] (b) [Black] Hori et al.,[31] Hori et al.,[36] [Red] Peterson et al.,[37] Kuhl et al.,[30] Montoya et al.,[38] [Blue] Kortlever et al.,[39] [Purple] Cheng et al.,[40] Lum et al.,[41] [Orange] Feaster et al.,[42] Liu et al.,[43] [Green] Garza et al..[44] Copyright © 2022 Elsevier Ltd, Copyright © 2019 Springer Nature Limited and American Chemical Society.

occurs simultaneously, this reduces the current efficiency of eCO_2RR.[58]

Table 2 shows the reactions involved along with the associated standard potentials for the formation of some known products under ambient conditions.[35] Since the C=O double bond is strong compared to C–O, C–H, or C–C bonds, CO_2 must overcome a large activation energy to initiate eCO_2RR.[59,60] The reaction begins with the formation of the CO_2^- radical. The potential of −1.90 V versus reversible hydrogen electrode (RHE) required for this reaction represents a large thermodynamic

Table 2. Thermodynamic potentials (E°) for eCORR and eCO_2RR in aqueous solutions (V vs RHE) at 1.0 atm and 25 °C.

Reaction	Number of electron transfer	E° (V) vs. RHE	Product
$CO_2 + e^- \rightarrow CO_2^{<MI><M->}$	1	−1.90	Key intermediate
$2H_2O - 4e^- \rightarrow O_2 + 4H^+$	4	+1.23	OER
$2H^+ + 2e^- \rightarrow H_2$	2	0.00	HER
$\boldsymbol{xCO_2 + nH^+ + ne^- \rightarrow Product + yH_2O}$	**CO_2 Reduction**		
$CO_2 + 2H^+ + 2e^- \rightarrow CO + H_2O$ (1)	2	−0.10	CO
$CO_2 + 2H^+ + 2e^- \rightarrow HCOOH$ (2)	2	−0.12	HCOOH
$CO_2 + 4H^+ + 4e^- \rightarrow C + 2H_2O$ (3)	4	+0.21	C
$CO_2 + 6H^+ + 6e^- \rightarrow CH_3OH + H_2O$ (4)	6	+0.03	CH_3OH
$CO_2 + 8H^+ + 8e^- \rightarrow CH_4 + 2H_2O$ (5)	8	+0.17	CH_4
$2CO_2 + 12H^+ + 12e^- \rightarrow C_2H_4 + 4H_2O$ (6)	12	+0.08	C_2H_4
$2CO_2 + 12H^+ + 12e^- \rightarrow C_2H_5OH + 3H_2O$ (7)	12	+0.09	C_2H_5OH
$2CO_2 + 14H^+ + 14e^- \rightarrow C_2H_6 + 4H_2O$ (8)	14	+0.14	C_2H_6
$3CO_2 + 16H + 16e^- \rightarrow C_2H_5CHO + 5H_2O$ (9)	16	+0.09	C_3H_6O
$3CO_2 + 18H + 18e^- \rightarrow C_3H_7OH + 5H_2O$ (10)	18	+0.10	C_3H_8O
$\boldsymbol{xCO + nH^+ + ne^- \rightarrow Product + yH_2O}$	**CO Reduction**		
$CO + 6H^+ + 6e^- \rightarrow CH_4 + H_2O$	6	+0.26	CH_4
$2CO + 8H^+ + 8e^- \rightarrow CH_3CH_2OH + H_2O$	8	+0.19	C_2H_5OH
$2CO + 8H^+ + 8e^- \rightarrow C_2H_4 + 2H_2O$	8	+0.17	C_2H_4

*All potentials are referenced against the RHE.

barrier.[17,61] From a kinetic point of view, higher overpotentials are required for the formation of hydrocarbons, mainly because larger kinetic barriers have to be overcome.[62]

Furthermore, C_2^+ molecules are often used as feedstocks for chemical synthesis due to their higher energy density in terms of mass and volume compared to C_1 molecules.[63] Nevertheless, there are some kinetic and thermodynamic challenges in the production of C_2^+ products: higher barriers required for C–C coupling and a large number of electrons to be transferred, which is kinetically undesirable. Studies show that the formation of C–H bonds by H* transfer to C_1 species is kinetically more desirable than C–C bonds, resulting in lower selectivity during eCO_2RR.[64]

1.2. Catalysts for eCO_2RR

Recently various types of catalysts including metals,[65] metal alloys (Cu alloys with Zn, Ga, etc.),[19] metal oxides (mixed metal oxides such as spinels),[66] metal–N complexes (Fe–N–C, Co–N–C, Ni–N–C),[67] organic complexes (metal porphyrins, phthalocyanines)[67] have been investigated to efficiently reduce CO_2 to value-added chemicals. Among them, copper remains unrivaled.[68–70] Table 3 shows the type of electrolytes, efficiencies of catalysts used, stability and some other properties of catalysts for eCO_2RR to CO in recent years. For C_1 products, FEs of more than 80% are reported with Ag- and Sn-based catalysts. A few methanol-selective catalysts were introduced with wide FEs between 30% and 89%. In contrast, the FSs of methane-selective catalysts were consistently below 50%, and Cu-based catalysts predominated. For C_2 materials, the FEs of C_2H_4 and CH_3OH were consistently lower. Recently, FSs of up to 80% have been reported.[71] However, the FE for n-C_2H_7OH remains low. The mentioned current density (J) is the current per unit area, which describes the amount of current flowing through a given area of the electrode surface. It is normally expressed in units of mA/cm^2. Current density is an important parameter in electrochemical systems as it indicates the rate of the electrochemical reaction taking place at the interface between the electrode and the electrolyte.

Figures 4(a–c) show the faradaic efficiencies for CO, CH_4 and C_2H_4 of Cu–Pd catalysts with different mixing patterns: ordered, disordered and phase-separated, respectively. The FEs of C_1 and C_2–C_3 materials as a function of current density are presented in Figures 4d and e, while their energetic efficiencies can be seen in Figures 4f and g. While Figure 4 illustrates the general catalytic trends, the data points were not obtained consistently. It was found that higher values for FE can be achieved with increasing current density. Nanostructure catalysts have significant advantages over bulk catalysts[72] and can have more active catalytic sites per volume.[73] It has become possible to expose the preferred surfaces of catalysts with a high density of active sites.[74] Nanocatalysts are also often much more tolerant to heteroatomic impurities than bulk catalysts.[75] Figure 4h presents the FEs for H_2, C_1 and C_2 products at different applied potentials via Cu_3N-derived CuNWs, while Figure 4i shows the FEs for C_2H_4 production from Cu wires and CuAg wires in CO_2 and $CO_2 + CO$.

Table 3. Overview of investigated catalysts for electrochemical CO_2 reduction to CO.

Catalyst	Cell type	Electrolyte	E (V) vs. RHE	J ($mAcm^{-2}$)	FE (%)	Stability (h)	Ref.
Fe–N_4–Graphene	H-cell	0.1 M $KHCO_3$	−0.60	2.6	81	11	[76]
Cu foil	H-cell	0.1 M $KHCO_3$	−0.8	10	60	4	[77]
N–Porous carbon	Flow cell	0.1 M $KHCO_3$	−0.95	1.2	77	2	[78]
N–3D graphene	Flow cell	0.1 M $KHCO_3$	−0.58	1.9	84	5	[79]
Ni–N–graphene	H-cell	0.5 M $KHCO_3$	−0.67	91	10	20	[80]
CN/WMCNTs	1 M KCl	Flow cell	−1.46	91	97		[81]
Co/CNT	0.5 M $NaHCO_3$	H-cell	−0.60	25	98	11	[82]
N–CNTs	0.1 M $KHCO_3$	Flow cell	−0.36	1.6	81	9	[83]
F–C	H-cell	0.1 M $NaClO_4$	−0.60	0.25	90		[84]
Ni–N–C	H-cell	0.5 M $KHCO_3$	−1.0	10.5	72	60	[85]
Co–N_2–C	H-cell	0.5 M $KHCO_3$	−0.51	18	93	59	[86]
Ni/Fe–N–C	H-cell	0.5 M $KHCO_3$	−0.70	9.6	97	31	[87]
Ni–N_4–CNT	H-cell	0.5 M $KHCO_3$	−0.91	57	96	29	[88]
Sn/N–C	H-cell	0.5 M $KHCO_3$	−0.60	1.70	90	23	[89]
N–Graphene nanoribbon	H-cell	0.5 M $KHCO_3$	−0.50	5.5	87.5	15	[90]
Co–N_5–carbon spheres	H-cell	0.2 M $NaHCO_3$	−0.70	6.1	98.5	11	[91]
Fe–N–C	H-cell	0.1 M $KHCO_3$	−0.60	5.0	84		[92]
CuO-derived Cu nanowires	H-cell	0.1 M $KHCO_3$	−0.60	0.5	50		[93]
Cu_2Cd/Cd/Cu	H-cell	0.1 M $KHCO_3$	−1.0	6.8	84		[94]

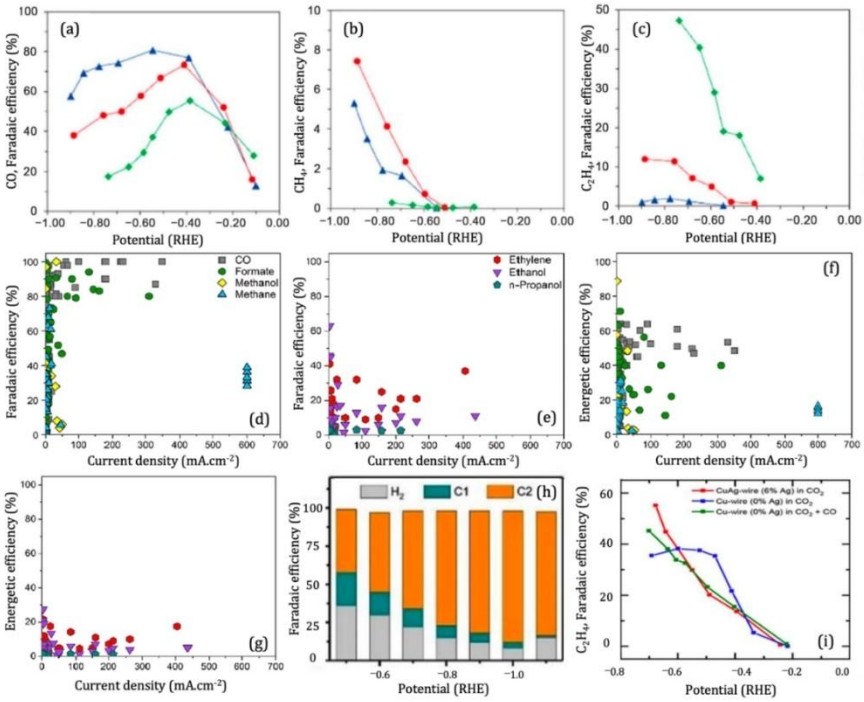

Figure 4. Faradaic efficiencies for CO (a), CH_4 (b) and C_2H_4 (c) of Cu–Pd catalysts with different mixing patterns (ordered, disordered and phase-separated, respectively). FEs vs current density for C_1 (d) and C_2-C_3 (e) products, and energetic efficiencies vs total current density for C_1 (f) and C_2–C_3 (g) products. FEs for H_2, C_1 and C_2 products at various applied potentials over Cu_3N-derived CuNWs. FEs for C_2H_4 production from Cu wires and CuAg wires in CO_2 and CO_2 + CO. Reproduced with permission from references.[98–102] Copyright © 2017 and 2018 American Chemical Society, Copyright © 2017 Elsevier Ltd, Copyright © 2019 Wiley-VCH Verlag GmbH & Co. KGaA, Weinheim Copyright © 2019, John Wiley & Sons, Inc.

1.3. Effects of Dopants and Promoters on eCO_2RR Performance

Cu-based catalysts have a significant drawback, namely the insufficient adsorption of key intermediates on the catalytic surface during eCO_2RR.[95] The incorporation of promoters into the catalyst serves to maintain the stability of the Cu surface and improve Cu dispersion, thereby promoting electron transfer to the active sites. This change in the binding properties of the surface adsorbents increases the activity of the catalyst.[96] The presence of dopants increases the number of reaction sites with different electronic properties and changes those of the host material, thereby promoting the adsorption strength of the intermediates.[97]

Experimental studies have revealed that the presence of a low concentration of dopants contributes to the formation of C_1 species.[103,104] Especially, the inclusion of metal dopants such as silver,[103,105] palladium,[103,106] platinum,[107] and zinc[103,108] in copper–M catalysts have been shown to increase the efficiency of production of C_1–C_2 products. Nabi et al. used DFT calculations to find a suitable catalyst for selective eCO_2RR to C_1 products (Figure 5a).[97] They examined the placement of various metals within Cu-based clusters and discovered that Cd- and Zn- doped Cu-based catalysts with monatomic doping were very effective for the conversion of CO_2 to CO. Conversely, core-shell catalysts with Ag, Pd and Pt in Cu-based compositions showed promising results for the production of HCOOH or HCHO. Deng et al. investigated the function of sulfur in a CuS_x catalyst using operando Raman spectroscopy and DFT simulations (Figure 5b–c).[109] They found that the high selectivity for formic acid was due to the presence of sulfur promoters on the copper electrocatalyst.

The DFT simulations showed that the S atoms over the catalyst surface weakened the adsorption strength of formate and carboxyl species. Consequently, CO production from carboxyl was suppressed, while the generation of $HCOO*$ from formate was favored.

Ye et al. developed a Sn–Cu catalyst and used it in the eCO_2RR to HCOOH (Figure 5d). Their results demonstrated that the Sn–Cu catalyst effectively suppressed the HER reaction, leading to a significant increase in the efficiency of HCOOH production.[110] Sarfraz et al. developed a bimetallic Cu–Sn electrocatalyst that effectively inhibited hydrogen adsorption on its surface, resulting in higher CO production efficiency (Figure 5e).[111] In their individual studies, Zeng et al. and Chen et al. investigated the use of Sn–Cu catalysts in eCO_2RR for CO production.[112,114] Zeng's findings emphasized the importance of incorporating Sn on the Cu foam electrode, resulting in an impressive efficiency of 94% (Figure 5f). Similarly, Chen et al. reported that the Cu–Sn electrode outperformed the Cu electrode in terms of FEs for both CO and C_2H_4 production. The efficiency of C_2^+ species production in eCO_2RR was enhanced by Fen et al. by incorporating lanthanides (Gd) into induced tensile-strained CuO_x catalysts (Figure 5g).[113] They performed extensive experimental and theoretical studies using DFT to elucidate the role of $Gd@CuO_x$ as a catalyst in eCO_2RR to C_2^+

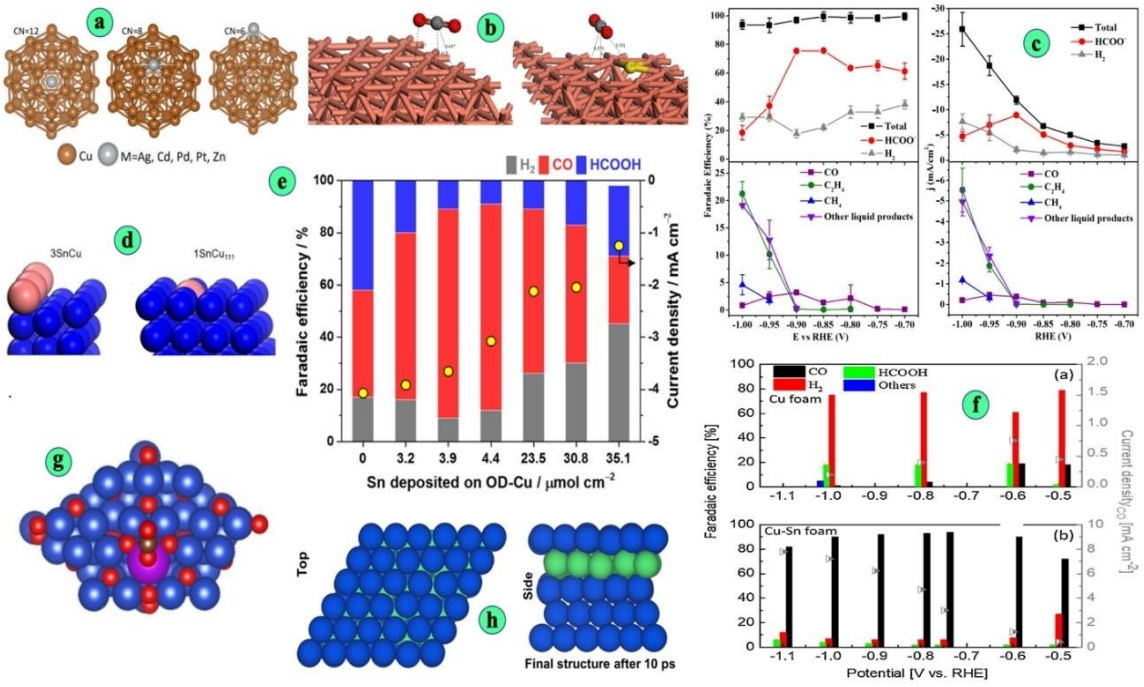

Figure 5. (a) Cu-based clusters doped with a metal atom at three different coordination sites,[97] (b) *CO_2 adsorption on Cu(111) and S-doped Cu (CuS) surfaces,[109] (c) faradaic efficiencies and current densities for CO_2 electroreduction products on the AC–CuS_x catalyst as a function of potential,[109] (d) structures of ^{3}SnCu(211) and ^{1}SnCu(111) catalysts,[110] (e) effect of Sn deposition amount on the OD–Cu on CO_2 electroreduction performance at −0.8 V (RHE) in 0.1 M $KHCO_3$ (pH 6.8),[111] (f) faradaic efficiencies of the major products and CO partial current densities at various potentials on Cu and Sn-dopped Cu electrodes,[112] (g) adsorption of *CO_2 over Gd_1-doped CuO_x surface,[113] and (h) optimized configuration of the Li-doped Cu(111) catalyst after 10 ps AIMD simulation.[95] Reproduced with permission from references.[95,97,109–113] Copyright © 2018 and 2019 Elsevier, Copyright © 2016, 2018 and 2023 American Chemical Society.

products. The results showed that Gd@CuO_x increased the stability of the key intermediate (OCCO). Moreover, the energy barrier associated with the transition from 2CO to O*CCO was found to be significantly affected by the tensile strain in Gd_1/CuO_x, contributing to its exceptional performance in eCO_2RR. At a potential of −0.8 V (RHE), the C_2^+ product exhibited a remarkable FE of 81.4%, accompanied by a partial current density of 444.3 mA cm^{-2}.

Tiwari et al. conducted a study in which an alkali metal-doped Cu(111) subsurface was introduced to investigate the influence of the promoter on the catalytic conversion of C_2H_6O to *n*-butanol (Figure 5h).[95] The process of transformation of C_2H_6O to *n*-butanol over the Li-doped Cu(111) catalyst was compared with the periodic Cu(111) catalyst. The Li monolayer transfers a considerable amount of charge to the upper layer of Cu(111), resulting in an electron-rich Cu(111) catalyst. This leads to a strong adsorption of intermediates adsorbed by O atoms over Li-doped Cu(111) compared to Cu(111), which facilitates the catalytic upgrading of C_2H_6O.

1.4. *e*CO_2RR Thermodynamics

The Gibbs free energy of the reaction is influenced by the applied potential. The standard thermodynamic potentials and the applied equilibrium potentials for the eCO_2RR to different products are listed in Table 2. The potentials mentioned represent the minimum energy required for product formation. It is important to highlight that the thermodynamic cell potential of a product indicates the minimum energy required for economic viability in terms of energy costs. This emphasizes the difference between the thermodynamic minimum and the actual operating conditions in eCO_2RR.[115–118] The OER reaction ($2H_2O \rightarrow O_2 + 4H^+ + 4e^-$) acts as an electron source and contributes to the overall reaction of $xCO_2 + yH_2O \rightarrow \text{product} + zO_2$.[39] Since CO is a key intermediate, understanding its thermodynamic implications is essential for optimizing electrocatalysts and increasing the effectiveness of CO_2RR. The thermodynamics of eCO_2RR can be manipulated by controlling the CO binding energy on the catalyst surface.[119]

1.5. Challenges and Benefits of eCO_2RR

eCO_2RR offers considerable advantages:

- If the electrolyte is fully recyclable, only water and CO_2 gas are used.
- The modular properties of eCO_2RR show that a large-scale industrial production of a variety of fuels, alcohols, and hydrocarbons is possible.[120]
- The eCO_2RR reaction takes place at mild conditions (20 °C) and ambient pressure (1 atm) and is controlled by external parameters (i.e. U, applied potential).
- No additional CO_2 is emitted as long as the electricity is generated from renewable resources.

Despite immense progress, there is still no catalyst that has all the properties required for practical use. There are still some challenges:

- The conversion of CO_2 to CO_2^- has a high energy barrier that requires a large overpotential, resulting in a lower performance of the catalyst.
- A mixture of different gaseous and liquid products causes additional separation costs.
- Efficiency of eCO_2RR depends on the available active sites on the catalyst surface. Thus, the covering or blocking of active sites by intermediates and by-products, so-called catalyst poisoning, is a problem.[121,122] A maximum catalyst lifetime of 100 hours was observed for selective eCORR to ethanol,[123] while a maximum catalyst lifetime of 24 hours was recorded for eCO_2RR.[67]
- The effects of the HER side reaction should quench. The HER reaction occurs at low potential and can therefore have remarkable effects on catalyst selectivity and FE.[124]
- CO_2 has a low solubility of about 0.034 M at 25 °C, which negatively affects controlled reactions.[64] Possible remedies are the use of non-H_2O solutions, using high CO_2 pressure or low temperatures to increase CO_2 solubility.

1.6. Challenges with Multiscale Modeling

Modeling eCO_2RR is notoriously challenging because the process occurs at very different length and time scales, from the electronic structure of the catalyst to the design of a chemical reactor (Figure 6a,b).[125] Some of the key challenges in accurately modeling eCO_2RR are:

- **Complex reaction mechanisms**: eCO_2RR involves complicated reaction pathways with multiple intermediates. Identification and characterizing all relevant reaction steps and intermediates are a difficult task. In addition, modeling is further complicated by the presence of competing reaction pathways and side reactions.[126]
- **Reaction kinetics**: The activity of the catalysts, the rates of the individual reaction steps and the influence of factors such as surface structure, adsorption energies and reaction barriers are difficult to determine accurately.[127]
- **Electrochemical interface**: Modeling the electrochemical interface between the catalyst and the electrolyte is a challenge that requires sophisticated modeling techniques due to the interplay of charge transfer processes, double layer effects, and mass transfer phenomena. The distribution of adsorbates should not be considered uniform even if the length scale is small compared to the reactor, which is known as the mean-field approximation (MFA) approach.[128,129]
- **Experimental validation**: Another challenge is to obtain reliable experimental data to validate the models. The complexity of the reaction and the difficulty in accurately characterizing the reaction intermediates and kinetics make it a challenge to develop experiments that allow validation of the models.[35]

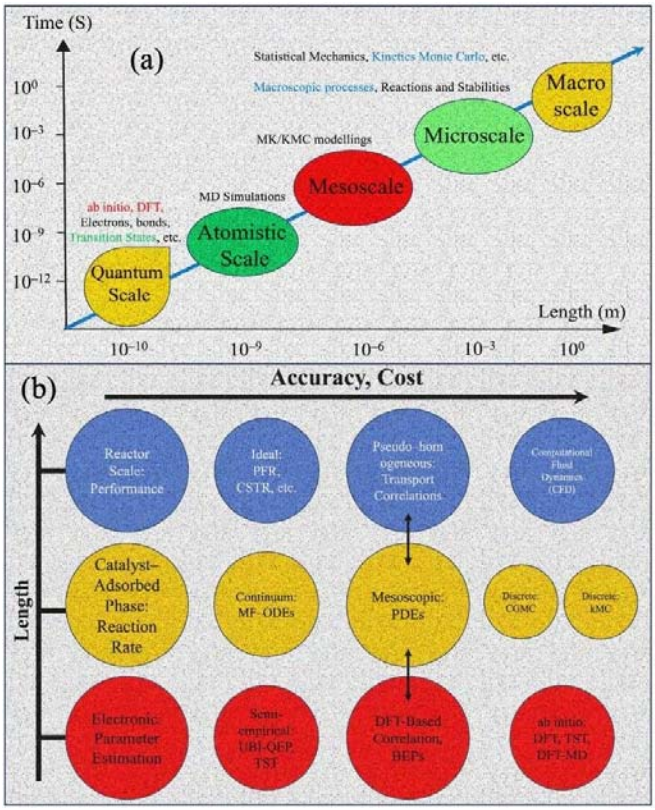

Figure 6. (a) An overview of different simulation methods used in multiscale modeling. (b) Schematic of three scales and a possible hierarchy of models on each scale. Accuracy and cost increase from left to right. Reprinted with permission from ref.[130] Copyright © 2011 Elsevier Ltd.

2. Modeling at Different Scales

Surface reactions differ from reactions in the gas phase, which are based on bimolecular collisions and energy transfer. The catalyst support has a significant influence on the reactivity of the catalyst as it changes the particle size, shape, electronic structure and interfacial composition. Catalysts interact dynamically with their environment and influence the kinetics of chemical reactions, a phenomenon that is not yet fully understood.[131] Multiscale modeling aims to incorporate these effects into practice. Multiscale modeling is used to develop robust models to predict the performance of Cu-based catalysts in industrial-scale reactors. This approach helps in the development of effective and efficient eCO_2RR processes.

This section provides a brief theoretical overview of multiscale modeling methods. The formation and breaking of bonds can be investigated using first-principles simulations of the electronic structure, such as DFT. Kinetic simulations reveal the evolution of the system over time based on all elementary reactions in the catalytic cycle, while continuum theories explain the role of heat and mass transfer at the macroscopic level, eventually leading to reactor-level CFD simulations and plant-wide simulations,[132] as shown in Figure 7. The results of the DFT calculations are used as input for the MK models or KMC simulations, which in turn lead to CFD.

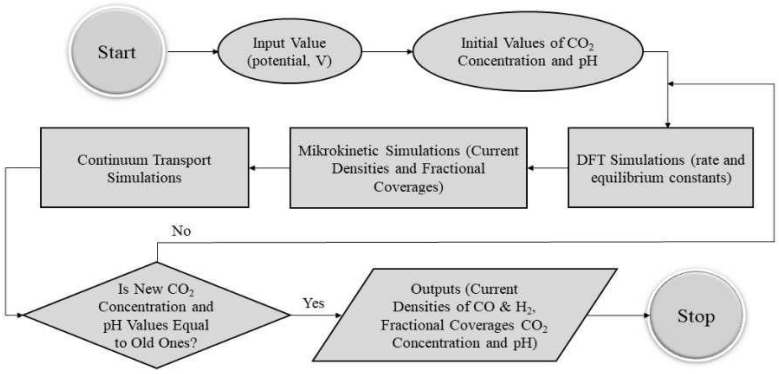

Figure 7. A schematic diagram of multiscale modeling including DFT, MK, and continuum transport model to predict partial current densities of CO_2 electrochemical reduction.

In the first step, the DFT simulations provide the energetic parameters needed to calculate the rate and equilibrium constants for each elementary reaction and adsorbent species. In the past, an intermediate post-processing step was performed to fit the DFT values to the finite temperature, pressure, potential and pH conditions in eCO_2RR.[133] However, newer methods have been developed, such as constant-potential (variable electron) modeling, which is implemented in the Grid Projector Augmented Wave (GPAW) package.[134] Constant-potential modeling in GPAW allows the direct simulation of electrochemical reactions at a specific potential, bypassing the intermediate step of post-processing. By explicitly including the potential in the calculation, this method enables the investigation of electrochemical processes under realistic conditions. It takes into account the effects of the applied potential on the electronic structure and reaction energetics and provides a more accurate representation of the electrochemical environment.

Compared to the previous method, constant potential modeling in GPAW offers a more streamlined and computationally efficient approach. It eliminates the need for extrapolations and corrections and provides more reliable predictions of reaction energetics and kinetics under specific electrochemical conditions.[134] In kinetic models, the reaction is described at the electrode level as a function of time. A continuum model is used to calculate the carbon dioxide concentration and pH at the cathode–electrolyte interface using the calculated partial current densities from MK simulations. A simulation sequence is repeated until convergence of CO_2 concentration and pH is achieved. In CFD, both the velocity and the flow parameters can be calculated to understand and analyze the behavior of fluids. Various methods are used in CFD for this purpose. A common approach is the FVM, which is known for its advantages in terms of memory utilization and solution speed, especially for large-scale problems.[135]

Theoretical prediction of electron transfer at the interface requires an understanding of the kinetics of electron motion at the electrode/electrolyte interface. Quantum mechanical models, especially DFT, provide insight into the electronic structure and energy levels of the electrode material and adsorbed intermediates. These models can predict the activation energy barriers for electron transfer processes, which are crucial for determining the rate constants of electrochemical reactions.[136] In addition, molecular dynamics simulations that incorporate quantum mechanics can capture the dynamic nature of the interface under operating conditions, providing a detailed view of electron transfer pathways. The impedance behavior of a planar electrode is closely related to the kinetics of electron transfer at the interface and the structure of the EDL.[137] Classical electrochemical theories, such as the Butler-Volmer equation, describe the relationship between the current density and the overpotential, taking into account the effects of the EDL. The EDL, which is formed by the arrangement of ions on the electrode surface, influences the capacitance and impedance of the system.[138] Classical models, including the Gouy-Chapman-Stern model, describe the distribution of ions in the EDL and their effects on the electrochemical behavior.

However, classical models often simplify the complex interactions at the molecular level. Quantum mechanical approaches, such as ab initio molecular dynamics, provide a more accurate description by taking into account the electronic structure of the electrode and the discrete nature of the solvent molecules and ions. These models can predict the potential of zero charge (PZC) and the differential capacitance of the EDL, which are crucial for understanding the impedance response. The combination of quantum mechanical insights with classical electrochemical theories enables a comprehensive understanding of interfacial phenomena and the development of accurate models to predict the impedance response and electron transfer kinetics of planar electrodes.[139]

In summary, the integration of quantum mechanical and classical theories improves our ability to predict the electron transfer at the interface and the impedance response of planar electrodes. Quantum mechanical models provide a detailed insight into the electronic structure and dynamic behavior of the interface, while classical theories provide a macroscopic understanding of the EDL and its effects on electrochemical performance. This combined approach is crucial for the development of advanced electrocatalysts and the optimization of their performance in eCO_2RR.[140]

2.1. Quantum Chemistry Calculations (Electronic Calculations)

A multiscale model for eCO_2RR starts at the atomic scale and is efficiently described by DFT. As the DFT scale is described in detail in numerous articles, it will not be discussed again in detail here. Due to the non-analytical computability of the wave function, approximations are used. Xu and Nitopi et al. provided a comprehensive review of theoretical methods and modeling strategies for electrochemical catalysis processes.[141,142] DFT calculations are used to improve the design of catalysts and increase their selectivity for multi-carbon products, which are economically more valuable compared to simpler products. While, MD calculations are used to understand how various environmental conditions (T and P) and catalyst modifications (dopants and defects) affect the activity and stability of Cu-based catalysts.

2.1.1. Computational Hydrogen Electrode (CHE) Model

The CHE model of Nørskov et al.[143] calculates the adsorption energies of individual adsorbates within a reaction pathway characterized by Proton-Coupled Electron Transfer (PCET) processes.

The CHE model calculates the free energy change (ΔG) for each step of an electrochemical reaction as a function of the applied potential (U). The equation used is: $\Delta G(U) = \Delta G(U=0) + neU$. Where $\Delta G(U=0)$ is the change in Gibbs free energy at a reference potential of 0 V relative to the reversible hydrogen electrode (RHE), n is the number of electrons and protons transferred in the reaction step and U is the applied potential. The term U_L, which is the upper limit or thermodynamically limited potential for a reaction step, is the potential at which the Gibbs free energy change for that step becomes zero. Mathematically, U_L can be expressed as follows: $U_L = -\Delta G(U=0)/ne$. This relationship states that U_L is the potential at which the driving force for the reaction step is maximized under the given conditions, making the reaction thermodynamically favorable. It establishes an upper limit for the applied bias beyond which the reaction will not proceed spontaneously under standard conditions.

More specifically, U_L identifies the critical potential at which the change in Gibbs free energy for the specific step is zero, indicating equilibrium. Any additional potential beyond U_L would make the step exergonic. Other steps in the overall reaction pathway may have other changes in Gibbs free energy values, which may include endergonic (non-spontaneous) steps. However, these may be driven by the overall favorable free energy changes of the coupled steps in the reaction pathway. The statement that U_L is determined from the Gibbs free energy changes of the potential-determining step by the formula $U_L = -\Delta G(U=0)/ne$ thus provides a clear understanding of the thermodynamic limits and the maximum achievable driving force for a given electrochemical reaction step under the applied bias voltage.

PCET steps with negligible kinetic barriers allow easy overcoming under ambient conditions and determine the overall reaction kinetics based on energy differences between successive PCET steps. The CHE model is ideally suited to generate multi-step PCET reaction profiles without considering kinetic barriers and helps to identify the potential-determining step. This analysis, which is possible at any potential without additional computational cost, takes solvents and electric fields into account. However, the model overlooks biases and electrolyte-induced changes in the electronic structure and kinetics of the adsorbates.

The CHE model does consider solvent and electric field effects, but these are treated as general parameters rather than specific interactions with electrolyte components. This is the main difference between the way the model deals with solvent and electric field effects and the way it overlooks electrolyte-induced changes.

2.1.2. Constant Electrode Potential (CEP) Model

Although the CHE model is easy to use, it does not consider fluctuations in the electrode potential, which leads to inaccuracies in the estimation of the reaction and activation energies. The CEP model overcomes the limitations of the CHE model by using a self-consistent approach.[144] This involves adjusting the number of electrons in the unit cell to allow fractional values that match the Fermi level (E_F) with the desired electrode potential. The E_F energy is iteratively tuned to achieve a target value during geometry optimization. Consequently, the work function (Φ) and the electrode potential (U) remain constant during the electrochemical reaction. The U value of the electrode can be determined by relating the Φ value of the system to the experimentally measured work function of the standard hydrogen electrode (SHE, 4.43 eV) using the equation $U = (-E_F - \Phi_{SHE})/e$. This value was used by Anderson et al.[145,146] in their studies of various electrochemical interfaces and agrees with the experimentally determined value in the range of 4.2 ± 0.4 eV.[147]

Both the CHE and CEP models are used to study electrochemical reactions, especially those involving hydrogen. Both models incorporate the concept of electrode potential and take into account the adsorption of reaction intermediates. However, they differ in the treatment of the adsorption coverage and the variation of the electrode potential. In the CEP model, the electrode potential is directly related to the adsorption coverage of the reaction intermediates, so that the coverage of the catalyst surface must be specified. In contrast, the CHE model does not explicitly consider the adsorption coverage and assumes a constant electrode potential that is not influenced by adsorbed intermediates. Interestingly, the CEP model reduces to the CHE model when the coverage approaches zero, as the adsorbed intermediates no longer influence the electrode potential. Thus, while the CEP model provides a more detailed description by taking into account the effects of adsorption coverage on the electrode potential, the CHE model provides a simpler description with a constant electrode

potential. However, both models converge to the same description in the limiting case of zero coverage.

2.1.3. Solvated Jellium Method (SJM)

The SJM is a computational method used to simulate charged surfaces in the DFT.[148] It can be used at constant charge or, as described above, at a constant potential.[149] The SJM approach consists of two components: Jellium and an implicit solvent. The jellium component is a uniform background charge distribution representing the metal electrode, while the implicit solvent is added to the simulation to screen the large potential field that would be created by the excess electrons and the jellium countercharge. The SJM method has been used extensively in the study of electrocatalytic reactions.[148] Each method (CHE, CEP and SJM) has its strengths and limitations, and the choice of method depends on the specific requirements and complexity of the system under investigation.

2.1.4. Solvation Effects

Solvation effects play a critical role in shaping the reaction mechanisms and kinetics of eCO_2RR. The solvation shell surrounding the catalyst surface has a significant impact on the adsorption, diffusion and electronic structure of reactants and intermediates, thereby modulating the thermodynamics and kinetics of chemical reactions. One approach uses a full ab initio treatment that explicitly accounts for all solvent molecules in the solvent/solute system. While this approach provides the most accurate treatment, it requires significant computational resources due to the large number of solvent molecules required to capture the equilibrium properties and statistical averaging. The second approach uses implicit models with classical continuum approaches to model the electrolyte. These computationally feasible methods, in combination with a quantum QM treatment of the solute, provide accurate results because they adequately account for the interactions between the solute and the solvent. Implicit solvent methods have the advantage of continuous variation of the interfacial charge, allowing simulations at constant potential by iteratively adjusting the Fermi level to the desired bias. A well-known model in this category is the Linearized Poisson–Boltzmann/Polarizable Continuum Model (LPB-PCM),[150–152] which efficiently models the electrochemical interface and enables for bias-dependent calculations. The LPB-PCM model ignores specific molecular solvent and electrolyte effects and faces the challenge of placing ionic countercharges and accounting for variations in surface charge density and electric field along the reaction path.[153]

Theoretical studies of eCO_2RR have explored implicit solvent models with a continuum description of the ions,[144,154] explicit solvent models with multiple layers of water molecules,[43] and the H-shuttling approach with one or two water molecules for proton transfer from the surface.[154] In solvated models, the adsorbed H* species reacts directly with reaction intermediates, whereas in the shuttle model, H* shuttles between one or two water molecules, one of which transfers the H* atom to the intermediates. Using DFT calculations in combination with a global optimization algorithm, Ludwig et al. revealed a significant and adsorbate-specific effect on the local water structure at the metal–water interface in explicit solvent models.[155] The study showed that solvation can stabilize various CO_2 reduction intermediates that are different from those observed in vacuum.

To achieve a balance between computational efficiency and accuracy, ad hoc solvation schemes have been developed.[156] These schemes are simplified models that effectively capture the essential features of solvation without requiring extensive computational resources. Continuous solvation models (COSMO, COSMO-RS) as common ad hoc solvation methods treat the solvent as a continuous dielectric medium with a defined permittivity and cavity shape representing the solute.[157] This approach efficiently captures the influence of the solvent polarity on the reaction energy. While ad hoc solvation models offer advantages in terms of computational efficiency, it is important to be aware of their limitations. These models are often based on empirical parameters that might not fully capture the specific interactions between the solvent and the reacting species in eCO2RR. Furthermore, they may not accurately describe solvation effects near the electrode surface, where the solvent environment is more structured.[158]

2.2. Kinetic Modeling

Atomic-level simulations provide insights into reaction steps and rates, while kinetic models simulate their interaction. KMC simulations are central to the study of how elementary steps influence conversion rates. The reversibility of these steps is crucial for effective KMC simulations, which use a stochastic approach to select and control the reaction steps. MK modeling goes one step further and uses differential equations to represent conversions and transport. A MK model incorporates kinetic parameters from quantum calculations, allowing a comprehensive assessment of the contribution of individual steps to the overall transformation rate. Typically, five steps are investigated, including the exploration of stable structures of adsorbed species, desorption of products, calculation of lateral interactions, conversion in reaction pathways and chemical conversions in the gas phase without catalysis.

KMC is increasingly used in the field of heterogeneous catalysis. By integrating KMC simulations with first principles calculations such as DFT, we can unravel complicated reaction pathways, identify bottlenecks and investigate durable outcomes such as catalyst deactivation. They also provide valuable kinetic parameters that can be used as input values for CFD simulations.[159] The use of KMC simulations makes it possible to determine the activity, selectivity and conversion rates of catalysts under operating conditions.[160,161] In KMC simulations, our goal is to solve the master equation:

$$\frac{dP_\alpha}{dt} = \sum_\beta W_{\alpha\beta}P_\beta - W_{\beta\alpha}P_\alpha \quad (4)$$

W denotes the probability that the system transitions from the α to the β configuration through reactions, while P represents the probability that the system is in an α configuration at time t. The forward and backward reaction constants of the elementary reactions can be determined by transition-state theory (TST). Kinetic modeling covers a range of processes including adsorption, desorption, surface reactions, homogeneous reactions, lateral interactions and catalyst evolution. This versatility makes it ideal for capturing phenomena such as catalyst deactivation, evaluating the effects of reaction conditions, analyzing reaction pathways and determining kinetic parameters that are important for CFD simulations.[162]

2.3. Molecular Dynamics Simulations

MD simulations use classical force fields to describe the interactions between atoms and molecules. This enables research into dynamic processes and the investigation of reaction mechanisms.[163] The accurate representation of the various species involved in eCO_2RR, including CO_2, reaction intermediates, products and the electrolyte environment, is crucial to gain reliable insights from MD simulations. In this context, the development and application of specialized force fields have played a crucial role.[164] Reactive force fields such as ReaxFF[165] and COMB[166] have been used to model the formation and breaking of chemical bonds during eCO_2RR, allowing the investigation of reaction pathways and the identification of key intermediates. Furthermore, polarizable force fields such as AMOEBA[167] and APPLE&P[168] were used to capture the electrostatic interactions and charge transfer processes, that are essential for an accurate description of the electrochemical environment and the adsorption of charged species on the catalyst surface. In addition, the integration of MD simulations with machine learning techniques has opened new avenues for the development of accurate and efficient force fields. Machine learning potentials, such as Gaussian Approximation Potentials (GAP) and Deep Potential Molecular Dynamics (DeePMD),[169] have been used to model CO_2RR systems and offer improved accuracy and transferability compared to traditional force fields.

2.4. Continuum Transport Model

CFD is an important tool for the fluid flow computation and has many engineering applications involving heat/mass transfer, pressure drop and more. CFD involves solving the fundamental equations of fluid dynamics, including the continuity, momentum and energy equations.

These equations form the basis for CFD and are crucial for predicting the flow behavior of fluids. Furthermore, CFD can be seamlessly coupled with reaction mechanisms by solving the continuum conservation equations for energy, mass and momentum in a multi-component fluid phase, allowing the numerical study of macroscopic mass and heat flow in a reactor. The Navier-Stokes equation serves as the basis for CFD and is used to describe many single-phase fluid flows.[178,179] Parameters such as temperature and mass fraction can be determined by additional equations once the velocity and pressure fields for the gas mixture are derived from the Navier-Stokes equation.[180]

3. Theoretical Studies on Different Scales

3.1. Overview of Multiscale Modeling of Chemical Reactions and Reactors

Various time and length scales are involved in electrochemical processes (see Figure 6b), which theoretical electrochemistry attempts to describe using a multiscale framework. In general, a single tool is used to simulate a process on a specific length and time scale. Figure 6a illustrates the main classes of calculation tools with their length and time scales. Multiscale modeling connects these different levels into a unified description and enables the derivation of macroscopic features from microscopic events. The interactions between the catalyst surface and the adsorbates, which lead to the potential energy surface (PES), the conversion entropy, the activation energy and the reaction energy, are described at the microscopic level. Using statistical mechanics, this information can be converted into the free energy of the reaction and finally into the rate constants.

Kinetic methods such as KMC or mean-field MK are often used to average the collective behavior in order to determine the reaction rate at the mesoscopic level, following the spatial and temporal evolution of the system. At the macroscopic level, concentration gradients, fluid flows and temperature differences can be observed. These can be tracked with CFD. It is worth noting that most multiscale models in the field of catalysis consider the coupling to be one-way, with the model at the lower scale passing the information to the model at the next higher scale. In a true multiscale model, however, the information flow is bidirectional, as the catalyst itself can change during the course of the reaction.

Multiscale models have been used to describe chemical processes in various fields.[181–183] Molecular modeling techniques, such as MD and KMC, are usually limited to short time and length scales. In KMC simulations, the time scale for the evolution of the simulated system can be seconds or even longer, while in MD simulations the time scale varies depending on the specific type of simulation.[184] In ab initio molecular dynamics (AIMD), the time scale is typically in the picosecond to nanosecond range, while in force-field-based MD it can be up to several microseconds.[185] In recent years, however, several coarse-graining approaches have been developed to perform molecular simulations for large systems. Coarse-graining reduces the number of degrees of freedom in a system, allowing the simulation of larger systems and longer time scales.[186]

These models have been used extensively to simulate complex molecular processes at a lower computational cost than all-atom simulations. ML techniques have also been used to develop coarse-grained molecular dynamics (MD) force fields.[187]

3.2. Electronic Structure Simulations

Electronic structure simulations can provide energetic parameters, ZPE energies, lateral interactions, charge distributions, partition functions, information on key intermediates, transition states (TS), the most stable structures and configurations, reaction mechanisms, and all other electronic parameters.[188–191] The DFT is most commonly used because of its favorable cost/performance ratio. The DFT calculations on eCO_2RR, including the catalyst materials, computation methods and parameters studied, are summarized in Table 4.

Table 4 provides a comprehensive overview of the efficiency of catalysts that have been used for eCO_2RR for various products in recent years. It not only gives an overview of the faradaic efficiencies of the different catalysts and shows their selectivity and performance in the production of various carbonaceous products, but also presents the standard thermo-

Table 4. Overview of Density Functional Theory investigations of CO_2 electroreduction.

Catalyst	XC Functional	Investigated Parameter	Main Outcome	Main Product	Computed Parameters	Ref.
Cu_2O	PBE	Reaction Mechanism	Proposed Mechanism ($CO^*\rightarrow CHO^*\rightarrow CH_2O^*\rightarrow CH_3O^*\rightarrow CH_3OH^*$)	Methanol	Work Function, Zero Point Energy (ZPE), Adsorption Energy, Activation Barrier, Charge Distribution	[129]
Co@Cu(100)	RPBE	Selectivity, Production Rate	• CO Formation Rate up to Twice as High Compared to Bare Cu • Cu Sites Near CO-poisoned Co-Atomic Sites Accelerate CO_2-CO Conversion	Ethylene	Catalyst Activity, Adsorption and Activation Energies	[170]
Cu–Ag Composite	PBE	Product Selectivity and Efficiency	Selective Ethanol Generation via Langmuir-Hinshelwood coupling at Cu–Ag boundaries	Ethanol	ZPE, Gibbs Free Energy Change, Entropy, HUMO, LUMO	[171]
Cu(111) Monolayers	GGA-PBE	Catalyst Selectivity (CH_3OH *vs* CH4), Reactions Pathway	Proposed Mechanism ($CO_2^*\rightarrow COOH^*\rightarrow CO^*\rightarrow CHO^*\rightarrow COH^*\rightarrow CHOH^*\rightarrow CH_2O^*\rightarrow CH_2OH^*\rightarrow CH_3O^*\rightarrow CH_3OH^*$)	Methanol	Formation Energy, Cohesive Energy, Adsorption Energy, Entropy and Phonon Dispersion	[172]
Copper/Indium	GGA-PBE	Selectivity and Stability	FE of ~93% at −0.6 to −0.8 V vs RHE and Stability of 60 h	Carbon Monoxide	Free Energy, Adsorption Energy, Activation Barrier, Charge Transfer	[173]
Stepped Copper	BEEF-vdW	Elementary Reactions Pathway, pH Effect	Proposed Mechanism ($CO^*\rightarrow OCCO^*\rightarrow OCCOH^*\rightarrow OCC^*\rightarrow OCCH^*\rightarrow C_2^+$)	C_2 Products	Adsorption Energy, Activation Barrier, Charge Transfer, ZPE, Free Energy Change	[43]
Cu(100)	PBE	Reaction Mechanism and Solvation Effect	Reaction Mechanism ($CO_2^*\rightarrow COOH^*\rightarrow CO^*+OH^*\rightarrow CO^*$) Lowest Kinetic Reaction Pathways for CO Formation and for $HCOO^-$ Formation are Quite Distinct	Carbon Monoxide and Formate	Adsorption Energy, Charge Transfer, Gibbs Free Energy	[174]
Cu(100)	PBE	Solvation Effect	• CO*–CO* Coupling is Most Kinetically Favorable in the Solvent Model • Ethylene Production Pathway ($CO^*\rightarrow OCCO^*\rightarrow OCCOH^*\rightarrow OCHCHO^*\rightarrow OCH_2CHO^*\rightarrow HOCH_2CH_2O^*\rightarrow CH_2CH^*\rightarrow CH_2CH_2^*$) • Ethanol Production Pathway ($CO^*\rightarrow OCCO^*\rightarrow CCO^*\rightarrow CHCO^*\rightarrow CHCHO^*\rightarrow CH_2CHO^*\rightarrow CH_3CHO^*\rightarrow CH_3CH_2O^*\rightarrow CH_3CH_2OH^*$)	Ethylene and Ethanol	Vibrational Frequency, ZPE, Free Energy, Adsorption Energy, Activation Barrier, Charge Transfer	[175]
Ultrasmall Cu Nanocrystals Dispersed in Nitrogen@C	GGA-PBE	Reaction Mechanism and Catalyst Efficiency	• Cu/NC-NSs have 43.7 and 63.5% Faradaic Efficiencies for the Synthesis of Ethanol and Formate with Applied Potentials of −0.37 and −0.77 V • Proposed Mechanism ($CO^*\rightarrow OCCO^*\rightarrow HOCCO^*\rightarrow CCO^*\rightarrow CHCO^*\rightarrow CH_2CO^*\rightarrow CH_3CO^*\rightarrow CH_3CHO^*\rightarrow CH_3CHOH^*$ $CH_3CH_2OH^*$)	Ethanol	Adsorption Energy, Activation Barrier, Charge Transfer, ZPE, Free Energy Change, Entropy, HUMO, LUMO	[176]
M@Cu(100) M@Cu(111)	PAW/PBE	Electronic Structures of M on the Adsorption	• The High Coverage of CO* Leads to Improved Activity of the C_2 Products • Adsorbed Key Intermediates Show Finely Tuned Binding Strengths Nearby	C_1 & C_2 Products	Stability, Adsorption Energy, Activation Barrier, Selectivity, Activity	[177]

dynamic potentials and the applied equilibrium potentials for eCO_2RR for these products. These data are crucial for understanding the minimum energy required for product formation and for assessing the economic viability in terms of energy costs. The information mentioned (catalytic efficiencies, Faradaic efficiencies, selectivity, and standard thermodynamic potentials) is scattered in different columns of Table 4 rather than in a single dedicated column. Mandal et al. used DFT to investigate methanol production from the hydrogenation of CO_2.[172] The focus was on evaluating the viability of Cu monolayer based catalysts compared to Cu(111) surfaces and Cu nanocluster (NC)-based catalysts for selective CO_2 hydrogenation. The results showed that the Cu(111) catalyst exhibited high selectivity for the production of methanol as opposed to methane, outperforming the previously known Cu-based catalysts. Moreover, the Cu(111) catalyst operated at a lower working potential (0.46 V) compared to the previously studied Cu(111) surface catalysts (0.71 V)[192] and Cu-NC-based catalysts (0.53 V).[193] The study revealed a selective pathway for the hydrogenation reaction in which the formation of CH_3OH occurs via the *CHO intermediate rather than the *COH intermediate, which leads to the formation of CH_4. These results emphasize the highly nucleophilic nature of the Cu(111) catalyst and indicate its potential as a selective catalyst for the eCO_2RR to methanol, outperforming previously studied Cu-based catalysts.

Hirunsit et al. performed DFT simulations to investigate the eCO_2RR over stepped surfaces of Cu-based alloys (Cu_3X) for methane and methanol production.[194] The aim of the study was to investigate the relationships between the CO adsorption energy, the adsorption energy of other important $C_xH_yO_z$ intermediates, the overpotential, limiting-potential elementary step, and the selectivity for methane and methanol. Their results emphasize the importance of the formation of the CH_2OH* intermediate and the preference for protonation of the C atom over the O atom in determining methanol selectivity. Interestingly, in contrast to previous observations on pure metal catalysts, the calculations indicated that the electroreduction activity on Cu-based alloy catalysts does not exhibit a volcano-type relationship. Table 5 displays the computed E_{ads} for all species and key intermediates in the cases of Mandal et al. and Hirunsit et al. on the catalysts used.

Zhao Q. et al. investigated competing pathways in eCO_2RR on Cu using the embedded correlated wave function (ECWF) theory method, outperforming current DFT calculations. Their findings validate that the initial step of eCORR via hydrogen

Table 5. Calculated adsorption energies of all intermediates during CO_2 electrochemical reduction to CH_3OH over Cu NC (nanocluster), $Cu_3Ir(211)$ and Periodic Cu(111) electrocatalysts.

Intermediates	Cu NC Catalyst, Rawat et al.[193]		Cu3Ir(211) Catalyst, Hirunsit et al.[194]		Cu(111) Catalyst, Mandal et al.[172]	
	Adsorption site	Adsorption Energy, Eads (eV)	Adsorption site	Adsorption Energy, Eads (eV)	Adsorption site	Adsorption Energy, Eads (eV)
CO_2*	Bridge-top	−1.14	Not adsorbed		Bridge	−0.21
H*	fcc	−2.71	Bridge	−0.66	Hollow	−3.52
O*	fcc	−5.21	Bridge	−0.16	Hollow	−5.26
OH*	fcc	−3.84	Top	−0.29	Hollow	−3.83
CO*	fcc	−1.10[a]	Top	−0.62	Top	−0.98[b]
HCOO*			Bridge	+0.30	Bridge	−3.60
HCOOH*					Top	−0.70
H_2COOH*					Hollow	−3.16
H_2CO*	Bridge-top	−1.66	Bridge	−0.64	Bridge	−0.35[b]
H_3CO*	fcc	−2.88	Bridge	−0.70	Bridge	−2.62
trans−COOH*	Bridge-top	−2.79[a]			Bridge	−1.84
cis−COOH*						
C*			Hollow	−0.12		
CH*			Hollow	−0.60		
CH_2*	fcc	−3.87	Bridge	−1.59	Bridge	−3.58
CH_3*			Top	−2.11		
COH*	fcc	−3.10	Top	−0.39	Hollow	−2.97
HCO*	Bridge-top	−2.21	Top	−0.57	Bridge	−1.57[b]
HCOH*	fcc	−2.35	Bridge	−0.36	Bridge	−2.41
H_2COH*	Bridge-top	−1.85	Bridge	−0.50	Bridge	−1.54
CH_3OH*	Top	−0.49			Top	−0.39
H_2O*	Top	−0.38				−0.33

[a,b] Key intermediates that determine catalyst performance.

transfer on Cu(111) leads to the formation of COH* and not CHO*. While the prediction in favor of COH* aligns with the DFT results, the two theories differ in their predictions of structural and mechanistic behavior, suggesting that other aspects of the CO_2 reduction mechanism need to be reconsidered.[195]

Extensive research has been carried out over a period of three decades to study the reaction mechanism of eCO_2RR over Cu electrocatalysts. Although significant progress has been made, some aspects of the process are still unclear. Ongoing research aims to fill these knowledge gaps in order to achieve a comprehensive understanding and improved performance of the catalysts. A major focus is to explore the role of intermediates in the catalytic process. While some intermediates have already been identified and characterized, there may still be unidentified intermediates with unclear functions and behaviors. The influence of catalyst morphology and composition on the reaction mechanism is another area of research. Different copper catalysts exhibit different catalytic performances, prompting researchers to investigate the relationships between catalyst structure, composition and activity to optimize their effectiveness.

Jiang et al. used DFT to investigate the facet dependence of C–C coupling in the initial stages of eCO_2RR over a Cu catalyst.[196] They found that two different facets of Cu catalysts, (100) and (211), exhibited the highest efficiencies in the production of C_2^+ chemicals. Confirming this result, their synthesized Cu nanoparticles with (100) facet exhibited efficiencies and partial densities of more than 60% and 40 mA cm^{-2}, respectively.[196] Using DFT simulations, Xiao et al. showed that the influence of active Cu^+ sites on the surface on the enhancement of eCO_2RR efficiency is limited and even leads to lower efficiency. In contrast, the model of metal embedded in an oxidized matrix (MEOM) shows a remarkable improvement in the kinetics and thermodynamics of CO_2 activation, which is mainly due to the synergistic effects resulting from the coexistence of active Cu^+ and Cu^0 sites on the surface.[197] Recent calculations by Gong et al. show that metallic Cu plays a key role in CO_2 activation and e^- transfer, while oxidized Cu can adsorb CO more strongly to enhance the rate of C–C coupling.[198] Chorkendorff et al. have listed possible reaction mechanisms of eCO_2RR over Cu electrocatalysts taking into account theoretical and experimental investigations (Figure 3b).[35]

Based on the reaction mechanisms illustrated in Figure 3b, there is general consensus that the adsorption of CO_2 is the rate-limiting step in eCO_2RR.[39] However, there is still uncertainty as to whether the CO_2^- radical and subsequently the COOH* intermediate are formed by a simultaneous transfer of protons and electrons or via a decoupled pathway.[39] Recent studies have revealed that both COOH* and OCHO* are significant intermediates in the conversion of CO_2 to CO and $HCOO^-$, as evidenced by different volcano patterns for their binding energies.[42] For example, a recent study using surface-enhanced Raman scattering (SERS) and DFT simulations showed that the initial intermediate in the generation of CO and HCOO over a Cu electrocatalyst is $*CO_2^-$. DFT demonstrated that $*CO_2^-$ is reduced to HCOO and CO by the activation of Cu–C and C–O bonds and the stabilization of Cu–O as the applied negative potential increases. It appears that the strength of Cu–C and C–O bonds are the most important factors determining the selectivity of the Cu electrocatalyst for CO and HCOO species.[199] In the production of C_{2+} species, CO* is the most important intermediate, but pH sensitivity plays an important role in deciding the selectivity between C_1 and C_2^+ products. Thus, C_2H_4 production takes place at a lower pH than CH_4 production.[18] Therefore, hydrogenation of CO and dimerization are thought to be the limiting steps in the formation of C_1 and C_2^+ species.[200]

Several aspects of CO dimerization remain unclear, including whether coupling occurs between two adsorbed CO or between an adsorbed molecule and a gaseous molecule. The question of whether CO coupling is an electrochemical or a purely chemical process is also unresolved.[144] Several studies have discussed the possibility of coupling intermediates and molecules such as CHO* and CO (gaseous) or CO_2 at larger overpotentials. This arises from the fact that two different paths lead to C_2H_4 depending on the configuration of the catalyst surface and the overpotential.[44,201] For example, some investigations have shown that the Cu electrocatalysts follow a low overpotential path for the dimerization of CO species above the (100) facets and a larger overpotential pathway above the (111) facets together with methane above CHO* as an intermediate, which is in good agreement with the higher selectivity of ethylene above the 100 facets.[44,201,202] Other reaction mechanisms such as the dimerization of CH_2 and CH_3, and the coupling of two hydrogenated CO intermediates to form C_2^+ products have also been proposed. Although these couplings are thermodynamically possible, the concentration of these intermediates is too low to be the main source of C–C bonds.[44,203] Some studies show that CH_2O* species contribute to the formation of CH_4 and CH_3OH as intermediates, e.g., $CHO^* \rightarrow CH_2O^* \rightarrow CH_3O^* \rightarrow CH_3OH/CH_4$.[50,204,205] Some parameters, including optimized configurations for CO_2*, COO_1H*, and COO_2H*, free energy profiles illustrating the formation of COO_1H* and COO_2H* together with the corresponding TS,[185] energy diagrams showing the eCO_2RR at U = 0 V, mechanisms of four different CO_2 reactions, forming either COOH or HCOO adsorbed on the surface by Heyrovsky or Tafel mechanisms,[206] high-resolution TEM of commercial Cu/C,[207] and DFT-calculated EP profiles averaged over the surface plane are presented in Figure 8.[185]

Figure 8 provides a comprehensive overview of the various computational techniques employed in the eCO_2RR investigation. Figure 8a shows the optimized configurations and the free energy profiles for the main intermediates involved in the eCO_2RR process as derived from DFT calculations. Figures 8b and c show the mechanistic insights from the DFT studies that elucidate the reaction pathways, activation barriers and the influence of Cu facets on eCO_2RR activity. In addition, Figure 8d shows a high-resolution TEM image of a Cu/C catalyst that combines the computational and experimental aspects. Figure 8e shows the electrostatic potential profile averaged over the surface plane, demonstrating the integration of electronic structure calculations with reaction modeling.

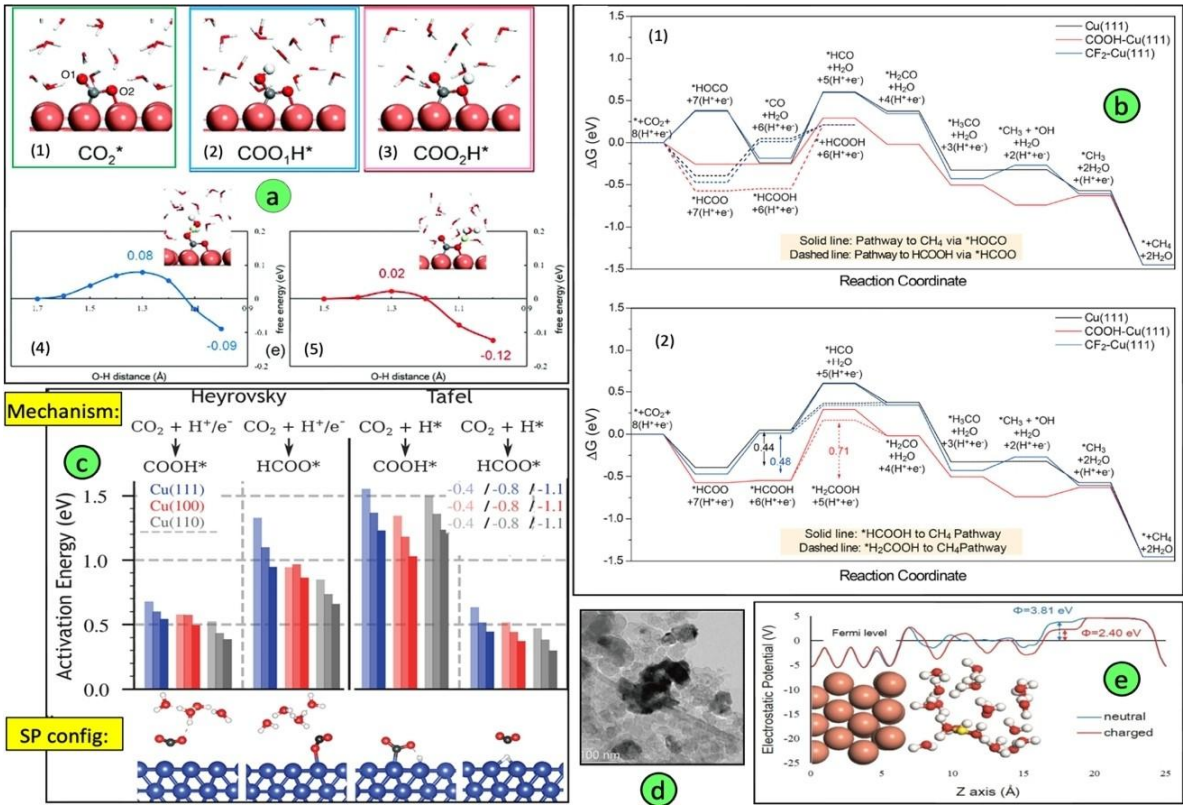

Figure 8. (a) Optimized configurations for (1) CO_2*, (2) COO_1H*, and (3) COO_2H*, Free energy profiles illustrating the formation of (4) COO_1H* and (5) COO_2H* alongside corresponding TSs,[185] (b) energy diagrams showing the eCO_2RR at U = 0 V and T = 298.15 K: (1) CO_2 transforms into CO and CH_4 via the HOCO* intermediate and to HCOOH* via the HCOO* intermediate, (2) CO_2 converts to CH_4 through the HCOO* intermediate,[208] (c) Top panel: mechanism of four distinct CO_2 reactions forming either COOH or HCOO adsorbed on the surface by Heyrovsky or Tafel mechanisms, Middle panel: histograms displaying computed activation energy for the four reactions on Cu(111) in blue, Cu(100) in red, and Cu(110) in gray at −0.4, −0.8 and −1.1 V_{RHE}, Bottom panel: atomic configurations of movable atoms in DFT calculations at saddle points for −0.8 V_{RHE} and Cu(111),[206] (d) high-resolution TEM of Cu/C,[208] (e) EP profile averaged on the surface plane.[185] Adapted with permission from references.[185,206,208] Copyright © The Royal Society of Chemistry 2017, and Copyright © 2021 American Chemical Society.

3.3. Molecular Dynamics Simulations (MD)

Recent studies in the field of eCO_2RR have increasingly utilized MD simulations to gain insight into the dynamic structural evolution of catalysts and its impact on eCO_2RR performance.[209–212] The identification of active sites and engineering during the dynamic evolution of catalysts are crucial to further improve the activity, selectivity and durability of Cu-based catalysts for high-performance eCO_2RR. Recent advances in the development of Cu-based electrocatalysts for eCO_2RR include tunable structure and size, the use of advanced supports, and the development of the composition of Cu-based oxides and alloys.[212–215] Future research should further explore the dynamic structure evolution of Cu-based catalysts and provide more insight into the theoretical explanation of the origin of the size and composition effects to support the design of highly efficient electrocatalysts.

For example, a study by An et al. investigated the structure-activity relationship of Cu-based catalysts with different sizes and compositions.[216] The study found that the Cu@CNTs catalyst exhibited higher activity for CH_4 production with a low overpotential value of 0.36 V compared to $CuNi_3$@CNTs (0.60 V), where CHO* formation proving to be the potential-determining step.

The effects of electrolyte composition and pH on the eCO_2RR process were also investigated using MD simulations. By simulating the solvation structure and dynamics of ions near the catalyst surface, researchers have gained insight into the role of the electrolyte in mediating CO_2 reduction kinetics and product selectivity. For example, in a study by Chen et al. the effect of electrolyte pH on the stability of reaction intermediates on Cu surfaces was investigated using MD simulations.[217] Their results showed the pH-dependent adsorption behavior of CO_2 and reaction intermediates and provided valuable information for the optimization of electrolyte conditions in CO_2 reduction systems. A key challenge in eCO_2RR research lies in the dynamic nature of catalysts under reaction conditions. In contrast to static models, MD simulations provide a powerful tool to capture the real-time evolution of catalyst structures during eCO_2RR. In a recent study by Qin et al., constant potential DFT calculations were used in the framework of MD simulations to investigate the sintering process of Cu single atoms in Cu–N–C single atom catalysts (SACs).[218] Their work showed that under eCO_2RR conditions, the Cu atoms can detach from the support material as Cu-$(CO)_x$ units and subsequently agglomerate into

clusters. Interestingly, the simultaneous adsorption of hydrogen and eCO_2RR intermediates such as CO was found to favor this sintering process. This study highlights the crucial role of MD simulations in elucidating the complex interplay between reaction intermediates and dynamic structural transformations in Cu-based catalysts. By elucidating the atomic-scale mechanisms underlying catalytic activity and selectivity, these MD simulations contribute to the rational design and optimization of Cu catalysts for efficient CO_2 conversion. However, further research is needed to overcome challenges such as accurate modeling of electrochemical interfaces and scalability of MD simulations to realistic reaction conditions.

3.4. Mesoscale Kinetic Simulations

A kinetic model is required to study the temporal development of the process. Although these are numerous, they are mostly phenomenological and aim to reconcile the experimental observations with an assumed mechanism. On the other hand, eCO_2RR has rarely been described at the MK scale using DFT data and then coupled with CFD simulations. In general, KMC or MK simulations can determine the rate-limiting step(s), chemical reaction pathways, key reaction intermediates, surface coverages, and the relationship between the rate-determining step (RDS) and reaction conditions.[219] While the mean-field approximation in MK modeling assumes that all adsorbents and intermediates are uniformly distributed,[220] KMC can account for lateral interactions and co-adsorbate effects. An overview of KMC/MK simulations of eCO_2RR including catalyst materials, computation methods (the KMC work packages employed), investigated parameters (e.g. pH effect, rate-determining step), etc. is summarized in Table 6. This table serves as a comprehensive tool to explore the effectiveness of catalysts in facilitating various electrochemical CO_2 reduction pathways and the feasibility of producing various carbonaceous compounds.

Recently, MK modeling has gained popularity to investigate polarization curves for eCO_2RR to explore reaction networks for feedstock generation.[221–224] As shown in Figure 9a, the Tafel slopes for one-C atom species are smaller than for two-C atom species, although physical nonideality must also be considered.[225] Chen et al. carried out MK modeling of eCORR on Cu(211) to illustrate the production of one-C atom species compared to two-C atom products in terms of Tafel slope and pH dependence.[43] As shown in Figure 9b, their analysis revealed that the first PCET of the OCCO* species was RDS for the production of C_2 products at low applied potentials, while the third PCET of the CHOH* species was RDS for the production of C_1 hydrocarbons, which is also evidenced by different Tafel slopes. The RDS step changes from PCET to OCCOH* for CO dimerization, while the first PES is characterized as RDS to produce C_2 products at large negative applied potentials. This leads to an increase in the Tafel slope for the production of one-C atom species, while the current density decreases for two-C atom species.

Hongjie et al. performed MK simulations on Cu catalysts for the $CO_{(2)}RR$ to study the predominant reaction routes leading to the production of CH_4 and C_2H_4.[233] They explored the reaction

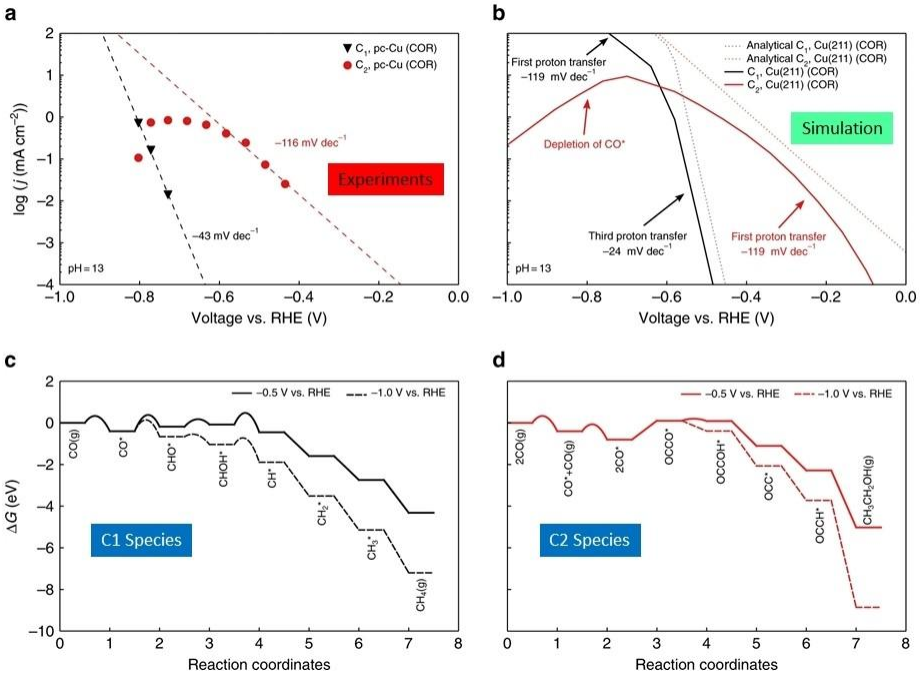

Figure 9. Plots of Gibbs free energy and polarization curves for one and two carbon atoms over copper electrocatalyst. (a) Experimental polarization curves of carbon monoxide conversion to C_1 and C_2 species over the copper catalyst (pH = 13, data from Reference[18]), (b) Expected polarization curves from the full MK model of carbon monoxide conversion to C_1 and C_2 species (pH = 13) over Cu(211), (c) Plot of Gibbs free energy for a dominant path at low coverage for C_1 products at −0.5 V and −1.0 V vs. RHE, and T = 298.15 K (d) Gibbs free energy diagram for dominant path at low coverage for C_2 products at −0.5 V and −1.0 V vs RHE and T = 298.15 K. Reprinted with permission from ref.[43] Copyright © 2019, Springer Nature Limited.

Table 6. Overview of Kinetic Monte Carlo/microkinetic investigations of CO_2 electroreduction.

Catalyst	Structure/Package	Main Outcome	Main Product	Computed Parameters	Ref.
Cu(100)	CatMAP Software Package, Four-Layer (3×3) Supercell	The Kinetically Most Important Step in the Formation of C_2H_4 is the Protonation of the O Atom in CHCO* to CHCOH* and the Subsequent dehydroxylation, Which Leads Exclusively to C_2HCs	C1 & C_2 Products	Selectivity, Role of the Electrolyte pH in Tuning Selectivity, Energetic Parameters, Surface Coverage	[226]
Cu Catalyst	Square Lattice (200 sites×200 sites) with Periodic Boundary Conditions	Product Largely Influences by the Active Site Size and the Total Surface Occupancy	C_2 Products	Rate Constants, Binding Energy, Sensitivity to Diffusion Rate, TOF	[227]
M@Cu(211)	MKMCXX Code/M Doped on a Four-Layer 3×3 Slab of Cu(211)	• Active Site for eCO_2RR is the Stepped M Edge • Primary Reaction Pathway COOH*→CO*→CHO* • Potential-Determining Step $CO^* + H^+ + e^- \rightarrow CHO^*$	CH_3OH & CH_4	Catalyst Activity, Energetic Parameters, Stability, Kinetic Parameters, Scaling Relations	[228]
Cu(111) & Cu(211)	MKMCXX Software Package	• H_2 Evolution Reaction Over Cu(111) • Stepped Cu(211) Surface is more Active than the Cu(111) Terrace for eCO_2RR	HCOO	Rate Constant, Diffusion Layer Thickness, Total Electrochemical Current, Faradaic Efficiencies, Selectivity, Surface Coverage	[229]
Cu(111)	CatMAP Software Package/(4×4) Cu-(111) Surface Unit Cell	The Intrinsic Dynamics Shown could be the Key to Explaining Why Copper is One of the Most Unique Metals in the Field of eCO_2RR	Hydrocarbons	Cyclic Voltammograms, Catalyst Activity	[230]
Cu(211)	CatMAP Software Package	• CO_2 Reduction at a Fixed pH Yield Similar Activities, Due to the Facile Kinetics for CO_2 Reduction to CO on Cu	C_2 Products	Tafel Slopes, pH Dependence, Activity, Surface Coverage	[43]
Cu(111)	A (3×3) Surface Unit Cell with a Four-Layer Slab (36 Cu atoms)	• HCOOH is the Main Product at Low Overpotential While CO Becomes the Main Product at High Overpotential • Increasing pH is Conducive to Improving the Faradic Efficiency of HCOOH Production and Suppressing the HER	CO & HCOOH	Reaction Rate, Applied Potential Dependency, Reaction Pathways, Product Distribution	[159]
Silver NPs	Customized MK Code, A 3×3×4 Surface	• Fluctuations in the pH value of the Cathode due to Pressure Changes have a Negative Effect on the HER • Changes in the Coverage of the Species on the Catalyst Surface have a Positive Effect on the eCO_2RR.	CO	Surface Coverage, Reaction Rates, Activity and Selectivity of CO Production	[231]
Single & Di-atom Catalysts	CatMAP Software Package	• Four MNCs as CrNC, MnNC, FeNC, and CoNC with High Catalytic Efficiency for eCO_2RR • Two C-atom Vacancies are the Most Stable Doping Site for MNCs	CO	TOF, Stability and Catalytic Activity, Coverage Plots, Activity Volcano Plots	[232]

mechanisms for one and two-carbon products using the available C atoms on the catalyst as probable intermediates. The MK modeling results show that CH_4 is formed via the COH* route followed by a C* intermediate in a wide range of potentials and pH values. As for the C_2H_4 route, the OC–C* pathway is predominant at neutral pH and potentials for C_2^+ species (−0.45 to −1.0 V, RHE) and transitions to the common OCCOH route at alkaline pH. They also found that *C–CO coupling and the hydrogenation of C* intermediates play a significant role in the competition for the production of one and two-carbon species in the neutral pH range. Their investigations reveal that the selectivities of C_2/C_1 species such as (511) > (100) > (211) > (111) can be facets of the copper electrocatalyst. The observations of Hori et al. on single crystal surfaces support these findings of Hongjie et al.[234,235]

MK simulations only consider the phenomena that take place on the catalyst surface. However, transport equations are required to accurately determine the concentrations of molecules and intermediates in the vicinity of the electrode. Meenesh et al. applied multiscale modeling to examine the CO production of CO_2 molecules over the Ag(110) catalyst, taking mass transfer effects into account.[132] Three reaction mechanisms (RM1, RM2, and RM3) were defined for the production of CO and COOH*. The protons were supplied from the H*, H_2O* or H_2O present in the electrolyte. It is noteworthy that $*CO_2^-$ was only included as a possible catalyst surface species in RM3. Meenesh et al. found that a correlation between current densities and CO_2 partial pressures could be reproduced exclusively by RM3 routes with the highest activation barriers for CO production.[236] They also showed that $*CO_2^-$ and COOH* species were the most accessible adsorbed intermediates, which was consistent with spectroscopic studies on Ag catalysts. This study concluded that the study of mass transfer effects allows a better reproduction of experimental trends in

partial current densities of CO and H molecules as a function of applied potential.

Various MK models are presented to explain the reaction kinetics for methanol production on Cu(100), Cu(110), and Cu(111) catalysts, including the RDS and selectivity control step and the most abundant surface species based on the studied reaction mechanism. The elementary reaction steps of the presented MK/KMC models of several pioneer groups are summarized in Table 7.

Jinghan Li et al. studied the effects of surface diffusion in eCO_2RR to multicarbon species over Cu electrocatalysts using KMC simulations.[227] A two-site (A and B) model was used to study the effects of surface diffusion on species with two carbon atoms (delta C-13) in eCO_2RR when the Cu electrocatalyst was co-fed with ^{13}CO and ^{12}CO. Since sites A and B had different selectivities for the production of hydrocarbons over oxygenates, there were differences in the C-13 content of these products. The measurement of delta C-13 with a mixed $^{13}CO + {}^{13}CO_2$ mixture may underestimate the actual site selectivity if the surface diffusion phenomenon is not considered. The size of the catalyst active sites and total surface occupancy significantly controlled the concentration of delta C-13, while the diffusion rate in the area with similar active sites and across the boundaries between areas was less sensitive as long as it was within a logical range for CO over Cu-based catalysts from previous studies. Figure 10 shows the role of important parameters with a significant effect on delta C-13 and a lesser effect on the isotopic fraction in the products. Figure 10a shows

Table 7. Summary of reaction network suggested by MK/KMC modeling.

Reaction ID	Elementary Reaction	Zijlstra B. et al. [229]	Nørskov J.K. et al. [237]	Chang Q. et al. [208]	Liu X. et al. [43]
R1	$CO_2(g) \rightleftharpoons CO_2^*$ (adsorbed)	*	*	*	*
R2	$H_2(g) \rightleftharpoons 2H^*$	*	*		*
R3	$H^* \rightleftharpoons H^*$ (diffusion)	*	*		*
R4	$H_2O^* \rightleftharpoons H_2O$ (g)	*	*		*
R5	$OH^* + H^* \rightleftharpoons H_2O^*$	*	*		*
R6	$CO_2^* + H^* \rightleftharpoons COOH^*$	*		*	*
R7	$CO_2(g) + H^* \rightleftharpoons HCOO^*$	*		*	
R8	$HCOO^* + H^* \rightleftharpoons H_2COO^*$	*		*	
R9	$H_2COO^* + H^* \rightleftharpoons H_2COOH^*$			*	
R10	$H_2COOH^* + H^* \rightleftharpoons H_2CO^* + H_2O^*$			*	
R11	$COOH^* + H^* \rightleftharpoons HCOOH^*$	*		*	
R12	$CO(g) \rightleftharpoons CO^*$		*	*	*
R13	$C^* + H^* \rightleftharpoons CH^*$	*			
R14	$CH^* + H^* \rightleftharpoons CH_2^*$	*	*		*
R15	$CH_2^* + H^* \rightleftharpoons CH_3^*$	*	*		*
R16	$CH_3^* + H^* \rightleftharpoons CH_4^*$	*	*	*	*
R17	$COH^* + H^* \rightleftharpoons C^* + H_2O^*$	*			
R18	$HCOH^* + H^* \rightleftharpoons CH^* + H_2O^*$	*			*
R19	$CH_2OH^* + H^* \rightleftharpoons CH_2^* + H_2O^*$	*			*
R20	$CH_3OH^* + H^* \rightleftharpoons CH_3^* + H_2O^*$	*			
R21	$CO^* + H^* \rightleftharpoons HCO^*$	*	*	*	*
R22	$CO^* + H^* \rightleftharpoons COH^*$	*	*		*
R23	$COH^* + H^* \rightleftharpoons HCOH^*$	*	*		*
R24	$HCO^* + H^* \rightleftharpoons HCOH^*$	*	*	*	*
R25	$HCO^* + H^* \rightleftharpoons CH_2O^*$	*	*	*	*
R26	$HCOH^* + H^* \rightleftharpoons H_2COH^*$	*		*	*
R27	$CH_2O^* + H^* \rightleftharpoons H_2COH^*$	*		*	*
R28	$H_2CO^* + H^* \rightleftharpoons H_3CO^*$	*		*	
R29	$H_2COH^* + H^* \rightleftharpoons CH_3OH^*$	*		*	
R30	$H_3CO^* + H^* \rightleftharpoons CH_3OH^*$	*		*	
R31	$CH_3^* + OH^* + H^* \rightleftharpoons CH_3^* + H_2O(g)$			*	
R32	$COOH^* + H^* \rightleftharpoons CO^* + H_2O(g)$	*			*
R33	$CHOH^* + H^* \rightleftharpoons CH^* + H_2O(g)$		*		*
R34	$O^* + H^* \rightleftharpoons OH^*$	*			

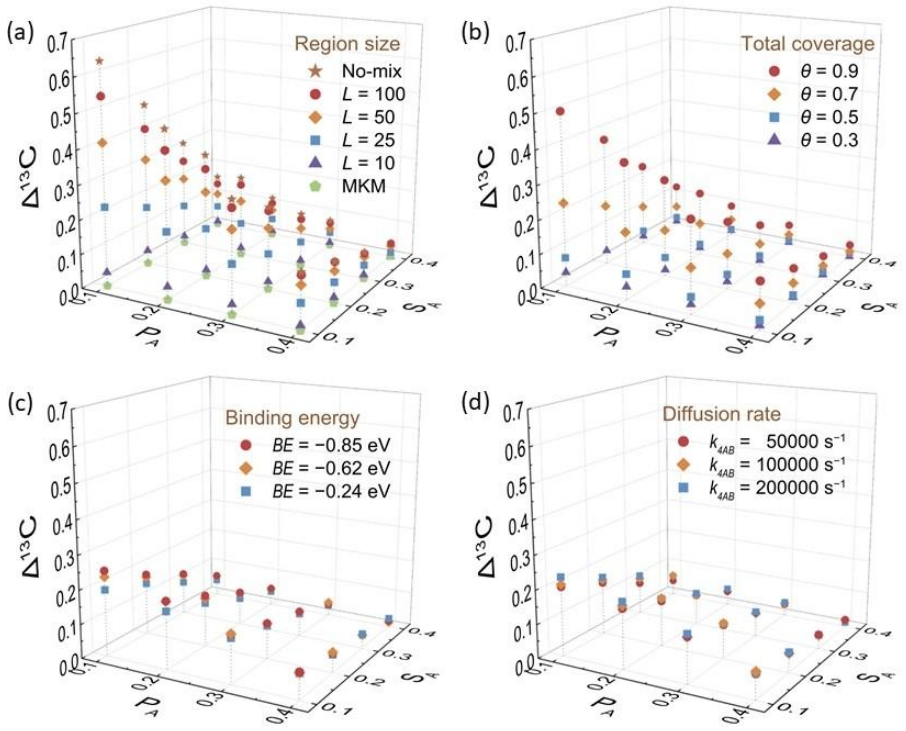

Figure 10. Factors significantly affecting delta C-13 rather than isotope fraction in products (a) KMC results for active site sizes L between 10 and 100 sites compared to MK model prediction ($\Delta^{13}C = 0$) and no-mixing limit, (b) KMC results with different total surface coverages (θ) for active site size L = 10. The coverage of CO* is 0.3, $k_4 = 3\times10^5\ s^{-1}$, and $k_{4AB} = 2\times10^5\ s^{-1}$ for all cases, (c) binding energy of CO* on Cu (BE) affecting the surface diffusion rate within areas A and B (k_4). The plots show the comparison for cases at −0.85, −0.62, and −0.24 eV, representing the facets with the highest CO* binding energy, Cu(100), and the facets with the lowest CO* binding energy, (d) diffusion rate constant across boundaries (k_{4AB}). L = 25 with a total coverage of 0.3 for all cases. The temperature serves as a proxy variable for the potential (E). To carry out electrocatalysis with negative potential, $T_{offset} = 10$ K is used and $T = E + T_{offset}$ is defined for the simulations. Adapted with permission from ref.[227] Rights managed by AIP Publishing 2019.

the results of the KMC simulation for active site sizes (L) between 10 and 100 sites compared to the projection of the MK model (C-13 = 0) and without mixing limit, while Figure 10b shows the results of the KMC simulation with various total surface coverages for active site size $L = 10$. Figure 10c shows that the binding energy of CO on the Cu catalyst affects the diffusion rate within areas A and B, and Figure 10d shows the diffusion rate constant across the boundaries.

3.5. Computational Fluid Dynamics Simulations

CFD simulations are performed to obtain information on the mass and heat transfer profiles, flow and pressure drop of the fluid in reactors under different operating conditions.[238–240] There are only a few studies using CFD simulations of the eCO_2RR process, usually with no or limited first-principles data as input. An overview of these studies, including the catalyst materials, calculation methods, investigated parameters, etc., is collected in Table 8. Table 8 provides a comprehensive overview of the studies using CFD simulations for the eCO2RR process, including the catalyst materials, calculation methods and parameters investigated. The studies listed in Table 8 show an improvement in mixing efficiency at higher flow rates as well as the recognizable trend of a gradual and linear increase in mixing efficiency over time at lower flow rates.

Jung et al. studied the relationship between the efficiency of a CO_2RR electrolysis cell and extrinsic properties using CFD simulations.[241] It was demonstrated that the uniform distribution of the flow pattern improves mass transfer through high convection and unidirectional flow patterns. They showed that the configuration of the flow channels plays an important role in facilitating the mass transfer, thereby increasing the production rate and stability. Their CFD simulation results showed that an increase in CO partial flow density was accompanied by an increase in convective mass transfer, proving that a high-performance design can be achieved by optimizing the flow pattern. This optimization increased the CO production rate by 28%. CFD simulations have shown that a lack of H_2O in electrolyzers with membrane electrode arrays can lead to limited mass transfer of ions and consequently lower eCO_2RR efficiency, confirming the important role of electrolyzer cell conditions.[242] Choi et al. developed a catholyte-free membrane electrode assembly (MEA) for eCO_2RR to C_2H_4.[243] At the same time, a CFD model for the CO_2RR electrolyzer was developed to investigate water management. Wet and dry CO_2 phases exhibited different catalytic performances, which was attributed to lower water activity on the catalyst surface. It was found that the formation of C–H bonds in eCO_2RR was mainly due to the H_2O transported through the membrane, while humidified water in the CO_2 feed affected the catalytic atmosphere and water activity, which altered the catalytic

Table 8. Overview of Computational Fluid Dynamics investigations of CO_2 electroreduction.

Catalyst	Package	Investigated Parameter	Main Outcome	Main Product	Computed Parameters	Ref.
Cu_2O Nanocubes	COMSOL Multiphysics	Substrate Effects on eCO_2RR Performance	A Substrate with High Porosity and Gas Permeability can Provide Unnoticed Gas Diffusion Pathway of Reactant CO_2 and the Intermediate Product, CO	C_2^+ Chemicals	Gas Diffusion, Velocity and Pressure Fields, Product Selectivity, Diffusion Rate, Total Current Density, Faradaic Efficiency	[244]
Cu Catalyst	COMSOL Multiphysics	Reactor Design and Understanding Governing Phenomena	Activation and Mixed-control Regimes Across a Range of Operating Conditions	C_2^+ Products	Identify Mass Transport Regime, Flow Rate and Electrochemical Potential	[245]
	Aspen HYSYS	A Kinetics-Mass Transport Model is Proposed to Explain the eCO_2RR-HER Competition	• eCO_2RR Influenced by both Concentration and Potential • HER Kinetics Only has Potential Limitation and Shows Lower Electron Transfer Capacity • $HCOO^-$ Faraday Efficiency Shows a Maximum Value with the Increasing Cathode Potential	Formate	Concentration Profile, Pressure Drop, CO_2 Conversion, Electroreduction Performance and H_2 Utilization	[246]
	COMSOL Multiphysics	Effect of Cathode Configuration on Electrocatalytic Activities	Velocity on the Anode Surface and in the Reactor Improve Efficiently Especially under Higher Inlet Velocities	Phenol Degradation	Velocity Profiles, Mass Transfer, Current-Potential	[240]
Ni Single-Atom (Ni–N/C)	COMSOL Multiphysics	Induce Different Water Contents in the Cathode Part	• Hydrogen Evolution Reaction became More Critical at Low Concentrations of CO_2 • Catalyst Exhibits a High Tolerance Toward Low CO_2 Partial Pressure (PCO_2)	Carbon Monoxide	Electrochemical CO_2R Performance, Faradaic Efficiency	[247]
Cu-*x*C		How Interfacial Wettability Impacts the eCO2RR Pathways to Ethylene and Ethanol	• Mass Transport of CO_2 and H_2O is Related with Interfacial Wettability • A C_{2+} FE of 80.3 % can be Achieved with a High C_{2+} Partial Current Density of 321 $mAcm^{-2}$	CH_3OH and C_2H_4	Controllable equilibrium of kinetically controlled CO* and H* by modification of alkanethiols with different alkyl chain lengths	[248]
Copper Nano-needles	COMSOL Multiphysics	CO_2 Electroreduction Acceleration to Multicarbon Products via Synergistic Electric–Thermal Field	Raising the Potential or Heating the Electrolyte Enhance C–C Coupling	Ethylene and Ethanol	Thermal Field Distribution, Velocity Profiles	[249]
	ANSYS Fluent	Fluid Flow of Carbon Dioxide (CO_2) via Polymeric Membrane	Gyroid Membrane is Slightly More Efficient than Flat-Sheet Membrane	C_2^+ Products	Geometry of Membrane System, Hydrodynamic Profile	[250]
Silver NP	ANSYS FLUENT	Effect of the New Flow Pattern on the Mass Transfer. Effect of the Extrinsic Properties on the Performance of a Large-Scale CO_2RR Electrolytic Cell.	Optimization of the Flow Pattern Improves the Production Rate of CO	Carbon Monoxide	Total Pressure Drops, Area Average Velocity, Partial Current Density	[241]

performance of eCO_2RR and HER. It seems that the anolyte provided most of the protons in the generated C_2H_4 rather than the humidified CO_2.

Jun et al. carried out CFD simulations to examine the effects of mixing efficiency of the micromixer in a flow microreactor on the synthesis of hierarchical Cu_2O octopodes with numerous step-like features (h-Cu_2O ONSs) at different flow rates.[251] They calculated the mixing efficiency at two different flow rates: 2.1 and 21 $ml\,min^{-1}$.

The results demonstrated a significant improvement in mixing efficiency at the higher flow rate, which reached 71 % in only 1.4 ms and 95 % in 5.4 ms. In contrast, the mixing efficiency at the lower flow rate of 2.1 $ml\,min^{-1}$ showed a gradual and linear increase over time.[251] This electrocatalyst showed superior performance in terms of partial current density and selectivity for ethylene formation in eCO_2RR compared to the cube-shaped Cu_2O catalyst. The h-Cu_2O-ONS catalyst, which has multiple step sites on its surface, exhibited a selectivity of 70 % FE for C_2^+ formation. Their results emphasize the importance of the stepped surface of Cu_2O nanocatalysts rather than their overall size. During eCO_2RR, the h-Cu_2O-ONS catalyst underwent surface restructuring and phase change, resulting in the formation of numerous grain boundaries between the coexisting Cu_2O and metallic Cu phases on its surface. This restructur-

ing was found to play an important role in promoting the selective formation of ethylene.

Choi et al. used CFD simulations to design a catholyte-free MEA for use in the eCO_2RR process.[243] They investigated the importance of water supply within the MEA for ethylene production using deuterium-labeled water. In their MEA model system, a catalyst electrode with Cu-based nanoparticles was fabricated and integrated into a MEA electrolyzer to enable C_2H_4 production via the eCO_2RR (as shown in Figure 11). Interestingly, the results showed that the protons responsible for C_2H_4 production came primarily from the anolyte and not from the humidified water through the cathode. This suggests that the dominant water flux from the anolyte serves as the main supplier of protons for eCO_2RR. To evaluate the effects of humidification, they compared the performance of the eCO_2RR under dry and wet CO_2 supply conditions. Their results showed that the formation of C–H bonds was primarily influenced by the water transported through the membrane. Furthermore, the presence of humidified water in the CO_2 supply affected the catalytic environment and consequently altered the performance of the eCO_2RR and the HER.

4. Coupling Different Scales

Until recently, most of the theoretical research on eCO_2RR has focused on single-scale modeling, mostly at the quantum level or kinetic simulations. Despite the increased interest in the reaction, a full-fledged multiscale model that includes DFT, MD, MK/KMC and CFD remains elusive. Multiscale modeling is usually limited to simple reactions and phenomena.[181,231,252] However, there have been several successful attempts to couple two scales in modeling eCO_2RR. For instance, Cheng et al. performed multiscale atomistic simulations to demonstrate CO_2 electroreduction to CO via gold nanoparticles.[253] They found that the NPs have excellent potential for eCO_2RR due to the abundance of active sites at the twin boundaries that disrupt the standard scaling relation. Liang et al. conducted a study coupling DFT and MD simulations to investigate the electrochemical reduction of CO* on Cu(111) and Cu on ZnO($10\bar{1}0$) surfaces.[254] The DFT calculations were utilized to evaluate the relative energies of the adsorbates to determine the reaction pathways on the investigated surfaces. To model a larger system size and non-zero temperatures and pressures, the researchers employed charge-optimized empirical many-body potentials (COMB) in the MD simulations. The results of the study revealed that the products observed during the MD simulations were similar to those measured experimentally, suggesting that the COMB potentials accurately capture the reduction chemistry despite the challenges associated with modeling electrochemical systems.

Liu and colleagues applied multiscale modeling to study CO production in a pressurized CO_2^- captured solution electrolyzer.[255] They integrated an atomic-scale DFT model to analyze each step of CO_2 reduction and HER, a mesoscale MK model to examine reaction dynamics, and a macroscale trans-

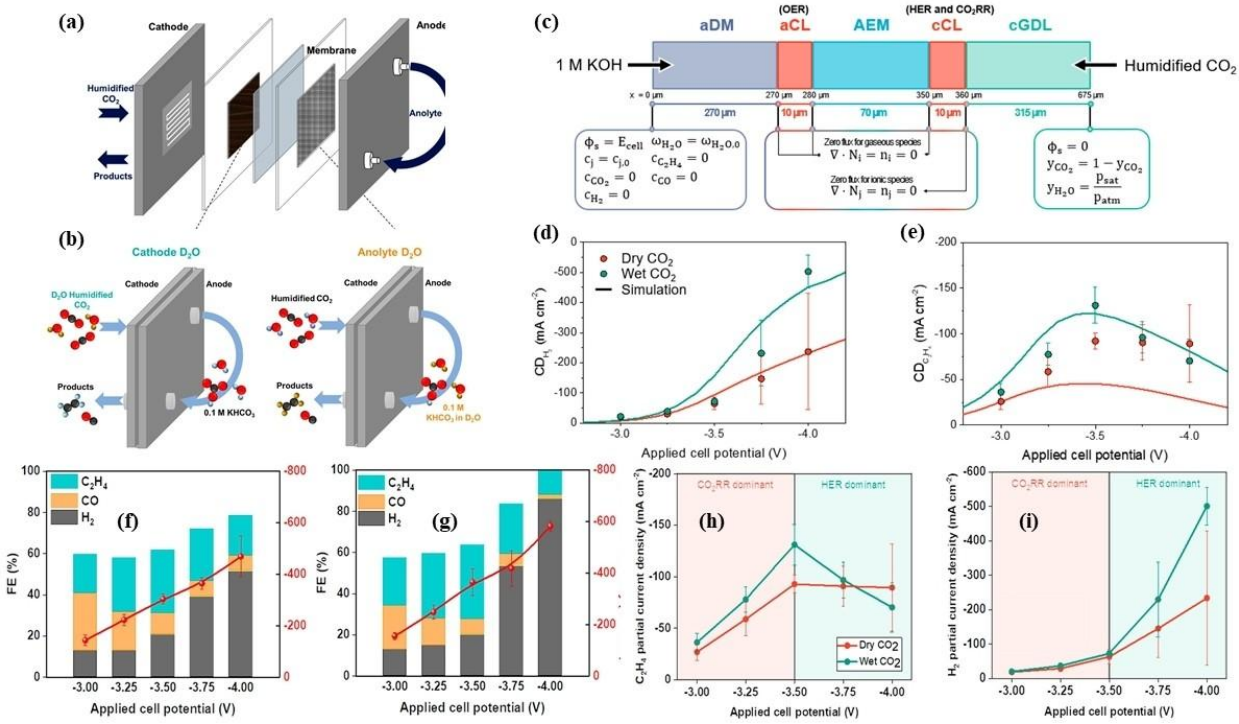

Figure 11. (a) the MEA Configuration, (b) experimental setup with humidified CO_2 supply and aqueous anolyte using the MEA CO_2RR electrolyzer, (c) boundary conditions applied across the different layers of the MEA, (d) variation in partial current densities of H_2 (e) of C_2H_4 as a function of applied cell potential using dry and wet CO_2 inflow at the cathode GDL (gas diffusion layer), (f and g) faradaic efficiencies and total current densities of dry and wet CO_2 supply depending on the applied cell potential, (h and i) partial current densities of C_2H_4 and H_2 with the dry CO_2 supply (cyan) and the wet CO_2 supply (red) as a function of the applied cell potential. Reprinted with permission from ref.[243] Copyright © 2022 American Chemical Society.

port model to evaluate species transport within the electrolyte and boundary layer. Their results indicate that the change in cathode pH due to pressure has a detrimental effect on HER, while the variation in species coverage has a favorable effect on eCO_2RR.

Singh et al. combined a DFT, MK and CFD model to gain a comprehensive understanding of the electroreduction of CO_2 on a silver surface. The eCO_2RR produced only CO and competed with the HER.[132] The combination of energetics and kinetics is a major challenge that is often overlooked in research. Hansen et al. investigated the dehydrogenation process of C_2H_6 on the Cu(111) electrocatalyst using MK models that included energetic information from DFT calculations.

Zijlstra et al. coupled DFT and MK modeling to investigate the effects of surface topology, solvation, and diffusion limitations on the current density potential curves and Faradaic efficiencies using a reaction-diffusion pattern during eCO_2RR over Cu(111) and Cu(211) electrocatalysts.[229] The stepped (211) surface of the copper electrocatalyst showed higher activity in the generation of formate, carbon monoxide and methane compared to the (111) surface. The presence of water molecules increased the selectivity for CO and CH_4 by facilitating the decomposition of carbon dioxide, supporting the activation step of CO_2 to carboxyl and suppressing the competing activation step to formate. At more negative potentials, the current densities increased, with CO and CH_4 identified as the main products. Figure 12 shows the TS geometries for the formation of COOH*, the calculated total electrochemical current and FE of the different products on the Cu(211) surface and Cu(211) in the presence of a catalytic H_2O molecule. The figure also contains potential energy diagrams showing the production of methane and methanol from HCOH at 0 V and −1.0 V (RHE). Nørskov et al. developed a kinetic model for the electrochemical reduction of CO, using ab initio methods and explicit solvent calculations to analyze the energetics of the elementary steps. Their model generated theoretical polarization curves, kinetic activity volcano and selectivities for different metals. Their findings revealed the predominant influence of the step sites on the CO reduction activity. They also identified an activity limitation determined by the scaling relation between the TS for CO hydrogenation and the CO binding energies. This discovery highlights a more stringent design criterion for the development of highly active catalysts for CO/CO_2 electroreduction that goes beyond the simplicity of conventional thermochemical analysis.[237]

Comparative polarization curves for Cu surfaces during eCORR to methane at pH = 7 are shown in Figure 13. It also shows activity volcanoes for certain transition metal surfaces at different potentials, revealing insights from MK modeling. In addition, Figure 13 shows the selectivity for COR at different

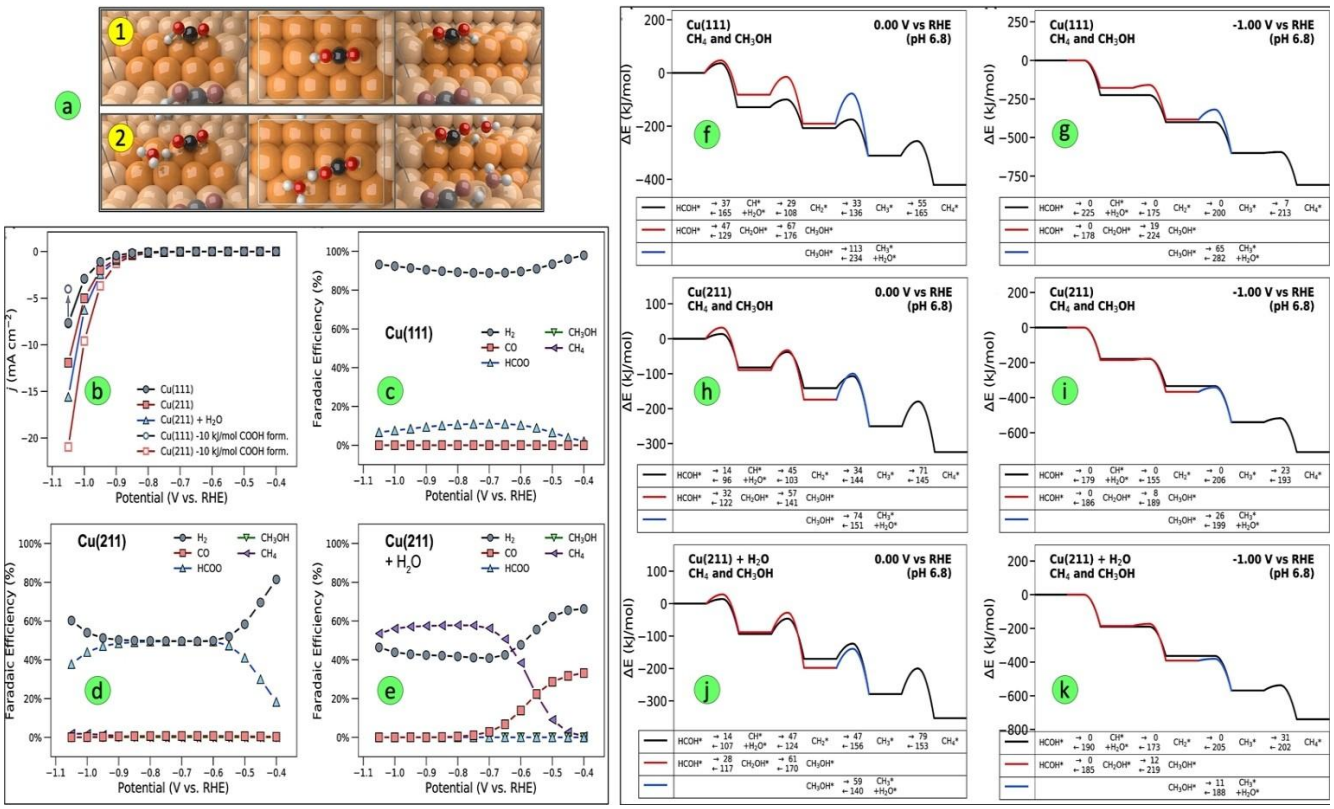

Figure 12. TS configurations determining the formation of *COOH on two different surfaces, (1) Cu(211) and (2) Cu(211) + catalytic H_2O molecule (a). MK simulations investigating the eCO_2RR on Cu(111), Cu(211) and Cu(211) + H_2O surfaces using a rotating disc electrode at 100 rpm and pH 6.8: total electrochemical current (b), FE of the different products (c–e). Potential energy diagrams showing the generation of CH_4 and CH_3OH from HCOH at 0 V and −1.0 V (RHE) on Cu(111), Cu(211) and Cu(211) + H_2O at pH 6.8 and T = 298 K (f–k). Three pathways are shown: (black) electrochemical HCOH hydrogenation to eliminate OH as H_2O, followed by CH hydrogenation leading to CH_4; (red) electrochemical hydrogenation of HCOH to CH_3OH; (blue) electrochemical CH_3OH hydrogenation to eliminate OH as H_2O. Adapted with permission from ref.[229] Copyright © 2020 Elsevier Ltd.

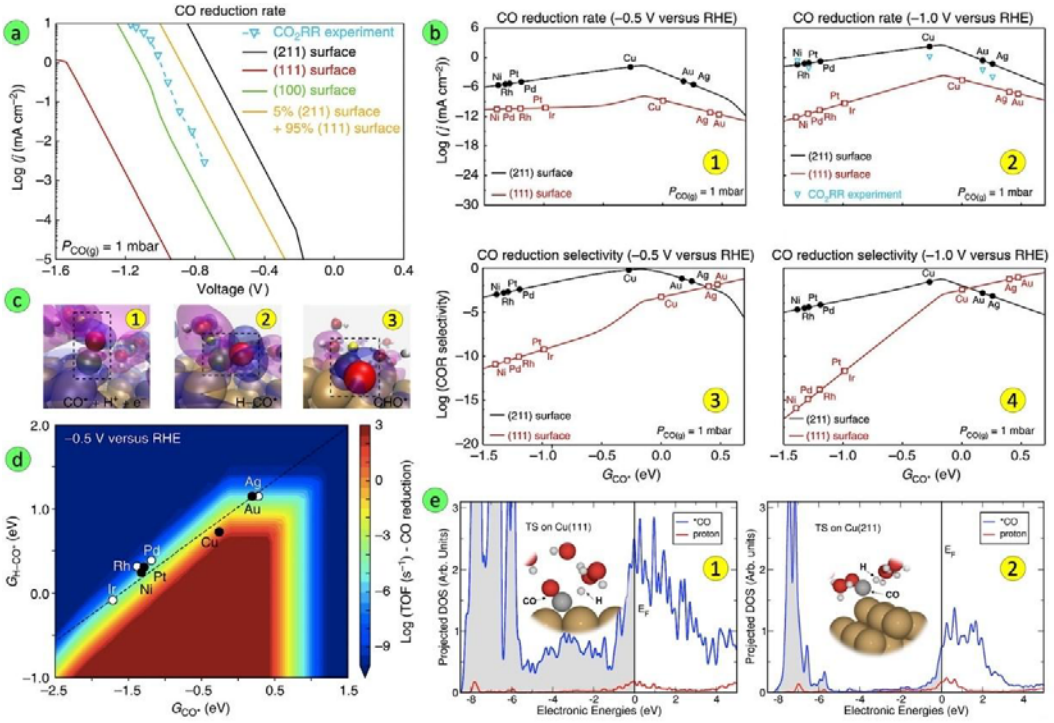

Figure 13. (a) Comparative polarization curves depicting the electrochemical behavior of Cu surfaces at pH = 7 with 1 mbar CO(g) for eCORR to methane on (111), (100) and (211) surfaces, (b) activity volcanoes for specific transition metal surfaces at different potentials (1) −0.5 V (RHE), (2) −1.0 V (RHE) as determined by MK modeling. Selectivity to COR at (3) −0.5 V (RHE), (4) −1.0 V (RHE), defined as the rate of COR relative to the sum of the rates of COR and HER, (c) (1–3) charge density difference isosurfaces representing the rate-determining proton-electron transfer to *CO to form *CHO. (d) Two-dimensional map illustrating the COR rate as a function of H–CO transition state energy and CO binding energy at −0.5 V (RHE). (e) Computed PDOS of the TS of CO protonation to CHO on Cu(111) and Cu(211) surfaces. Adapted with permission from ref.[237] Copyright © 2017, Springer Nature Limited.

potentials, isosurfaces of charge density differences illustrating rate-determining proton–electron transfer, a two-dimensional map depicting COR rate as a function of TS energy, and the computed projected density of states (PDOS) of TS of CO protonation to CHO on Cu(111) and Cu(211) surfaces.

The performance of electrochemical reactors can be significantly improved by developing more efficient electrochemical systems. The efficiency depends on the number of phases involved, the mode of operation (batch, continuous), and the electrocatalyst bed (fixed, fluid). Theoretical investigations to develop efficient reactors for eCO_2RR play an important role in addition to performing DFT and KMC simulations and enable experimenters to achieve higher efficiencies. Reactors for eCO_2RR are divided into fixed-bed, slurry and membrane reactors depending on the phases involved and the mode of operation. Due to mass transfer limitations and the need for post-process separation, slurry reactors are not economical despite their large surface area.[256] Fixed-bed reactors convert the products at higher rates, have low pressure drops and do not require separation of the catalyst from the products.[257] Continuous-flow reactors solve the mass transport restrictions by circulating reactants and products away from the electrode. Another strength of flow reactors is that they overcome the low solubility of CO_2 through the electrochemical reduction of gasses.[258] Therefore, a current density greater than 200 mA cm^{-2} using a gas diffusion electrode has been suggested in several articles.[259] For a full explanation at the macroscale, mass and heat transfer must be considered.

Research on multiscale modeling of eCO_2RR on electrocatalysts covering all scales is remarkably scarce. The complexity of this reaction, although not explicitly mentioned, could be the main reason for this scarcity. Most researchers have used DFT simulations to study the reaction mechanism of CO_2 reduction, determine theoretical overpotentials, etc.[260,261] They have also determined the selectivity, activity in terms of turnover frequency (TOF), surface coverage, and kinetic parameters using KMC simulations.[262,263] DFT and KMC scales have already been successfully linked in several research areas. Recently, the coupling of different scales has attracted increased attention in the field of CO_2 electroreduction.[237,264] However, there is currently no published research focusing on the direct coupling of CFD and KMC simulations, especially for eCO_2RR over Cu electrocatalysts. Most research in this area has focused on either CFD or KMC. For instance, numerous studies have used CFD to model the transport and reactions in eCO_2RR cells and reactors. Conversely, some research has used KMC to simulate the eCO_2RR mechanisms on catalyst surfaces. However, the challenge of directly integrating these models remains unresolved. The next step in multiscale modeling of eCO_2RR should be to focus more on successfully linking KMC/MK and CFD scales. The ultimate goal is to realize a comprehensive pattern that covers all scales, including DFT, KMC and CFD.

5. Machine Learning

The application of machine learning (ML) and artificial intelligence (AI) techniques to CO_2 reduction is also developing rapidly.[265–267] ML has been introduced as a way to improve catalyst design with higher efficiency and lower computational costs. Current ML algorithms for eCO_2RR use a large amount of existing information to learn from. Once these ML algorithms have undergone a training phase in which trends are identified using appropriate descriptors, they can suggest materials with certain capabilities without the need for new DFT simulations. Ulissi et al. developed a ML system to analyze plentiful arrangements of elements and active sites in intermetallic compounds.[268] Jiang et al. employed genetic algorithms to find stable solid–liquid interfaces on a copper electrocatalyst and used them to model the carbon monoxide reduction reaction to explain the solvation effect.[269] A neural network-based chemisorption model and scaling relationships were used by Xin et al. to predict 100 terminated catalysts for eCO_2RR to C_2.[270] Li et al. constructed a chemisorption model using artificial neural networks to accurately characterize the CO adsorption energies on the (100) surface of Cu-based catalysts for eCO_2RR. In this study, descriptors such as local electronegativity, effective coordination number, ionic potential, electron affinity and Pauling electronegativity were considered. By training the neural network model, they were able to predict the CO adsorption energies, which often showed good agreement with the results of the DFT calculations.[271]

In addition, there has been increasing interest in the application of new generations of force fields with machine learning in recent years. Zhang et al. have highlighted the potential benefits of integrating artificial intelligence into molecular simulations and have shown that this can lead to significant improvements in the field.[272] Machine learning has been shown to improve the accuracy of MD simulations, accelerate the development of better models and extend the reach of high-quality electronic structure theories.[273] This new approach has the potential to transform the way we study complex molecular systems and processes, offering new insights and opportunities for discovery. By combining the strengths of ML and molecular simulations, researchers can tackle challenging problems and gain new insights in a variety of areas.

6. Strategies to Increase the Activity of eCO_2RR on Cu

The eCO_2RR on Cu catalysts is a complex process that is influenced by several factors, including catalyst surface structure, reaction intermediates, and operating conditions. Here we summarize some strategies derived from theoretical modeling to improve the activity of eCO_2RR on Cu.

6.1. Tuning the Surface Structure of the Catalyst

The activity and selectivity of eCO_2RR on Cu strongly depend on the surface structure and exposed facets of the catalyst. DFT calculations have shown that stepped surfaces such as Cu(211) are more active than flat surfaces such as Cu(111) because they have undercoordinated sites that facilitate the adsorption and activation of CO_2. Shaping the surface structure to expose more active facets can increase CO_2 reduction activity and selectivity towards the desired products.

6.2. Alloying and Doping

Introducing foreign metal atoms into the copper lattice (alloying) or doping the surface with other elements can significantly change the electronic properties and improve the catalytic performance. For example, Cu-based alloys with metals such as Ag, Zn, Sn and Pd have been shown to improve efficiency and selectivity for various eCO_2RR products. DFT studies indicate that these modifications can stabilize key intermediates and reduce the overpotential required for CO_2 reduction.

6.3. Atomic Layer Deposition (ALD) and Core-Shell Structures

The creation of core-shell structures, in which a thin layer of copper is deposited over another metal core (or vice versa), can optimize catalytic properties by combining the advantages of both materials. ALD techniques allow precise control over the thickness and composition of these layers, which can be optimized based on theoretical models to increase activity and selectivity. Such structures can also help to reduce the formation of unwanted HER products.

6.4. Dynamic Restructuring of the Surface

Dynamic restructuring of the copper surface during eCO_2RR can lead to the formation of more active sites. Computational studies have shown that the in-situ formation of Cu(I) and Cu(0) sites during the reaction can improve catalytic performance. Controlling the potential and environment to favor these dynamic changes could be a strategy to increase activity.

6.5. Coverage and Adsorption Studies

Theoretical modeling shows that the coverage of reaction intermediates on the catalyst surface plays a critical role in determining the activity and selectivity of eCO_2RR. For example, a high coverage of CO intermediates is essential for the formation of multi-carbon products such as ethylene. Simulations show that maintaining optimal coverage of adsorbates through controlled reaction conditions can increase the production rates of the desired products.

6.6. Electrolyte Effects and pH Tuning

The choice of electrolyte and the pH of the reaction environment can significantly affect the performance of eCO_2RR. Theoretical studies suggest that alkaline conditions can suppress HER and favor CO_2 reduction, while certain cations in the electrolyte can stabilize the intermediates. The development of electrolytes based on these theoretical findings could lead to higher selectivity and efficiency in eCO_2RR.

6.7. Mechanistic Insights and Optimization of Reaction Pathways

Understanding the detailed reaction mechanisms and energy pathways for eCO_2RR on Cu can help identify the rate-limiting steps and optimize reaction conditions accordingly. Theoretical modeling provides insights into these mechanisms and enables the development of catalysts that can circumvent these limitations and improve overall activity.

6.8. Bimetallic Systems

Bimetallic systems can produce synergistic effects by altering binding energies and stabilizing key intermediates, thereby improving activity and selectivity.

6.9. Computational Screening of Promoters

Microkinetic modeling and DFT calculations can be used to screen potential promoters (e.g., ionic liquids, organic additives) that can selectively stabilize desired intermediates or reaction pathways, increasing activity for specific products.

By integrating these theoretical findings into the design and optimization of Cu-based catalysts, significant improvements in the activity and selectivity of eCO_2RR can be achieved. Future research should continue to utilize computational models to guide experimental efforts to develop more efficient and sustainable electrocatalysts for CO_2 reduction. These strategies guided by theoretical models can provide a roadmap for the rational design of Cu catalysts with improved eCO_2RR activity. They underscore the importance of a multilevel modeling approach that can capture the complex interplay of factors affecting eCO_2RR activity.

7. Conclusions and Future Perspective

Electrochemical CO_2RR has great potential as a cost-effective and environmentally friendly technology, provided that green electricity is available. Recent advances in available computing power have paved the way for purely theoretical studies. DFT, MD, MK/KMC and CFD simulations are used to explore parameters such as reaction mechanisms, determine rate-limiting steps and analyze mass and heat transfer profiles in reactors, with a focus on catalyst engineering and reaction conditions.

Despite the growing interest in eCO_2RR at different scales, there is still a lack of studies involving the coupling of CFD with DFT, MD and KMC scales. This is mainly due to the high cost and time required to perform numerous simulations, since the input values for KMC simulations depend on the results of DFT simulations and the input values for CFD simulations depend on the results of KMC simulations. In previous studies, these scales were usually coupled in pairs, e.g. DFT + KMC. Linking the DFT results to the MK/KMC scale is the first step towards multiscale modeling and can later be used as boundary conditions in CFD calculations. Multiscale modeling has its own implementation challenges due to the gaps between the scales. Most of the research work deals with the successful coupling of the DFT and KMC scales. Since the integration of DFT and KMC/MK is already well established, future research should focus on the coupling of MD and KMC/MK with CFD scales. This integration would allow the development of a comprehensive model encompassing all scales (DFT, MD, KMC and CFD). In parallel, a bidirectional coupling should also be considered, where information from the higher level is fed back to a lower simulation level. Only in such a case is it possible to consider the dynamic catalytic surface change.

The insights gained from this review of eCO_2RR with Cu can be strategically extended to other electrocatalytic reduction reactions. The fundamental principles of theoretical modeling as used for eCO_2RR are transferable to other systems. This review could also provide valuable directions for eCO_2RR on other catalysts as well as for other electrocatalytic reduction reactions such as the nitrogen reduction reaction (NRR),[274] the nitrate reduction reaction,[275] the NO reduction reaction,[276] etc. By integrating these perspectives, our review not only addresses the specific challenges of eCO_2RR on copper, but also sets a precedent for the improvement of other important electrocatalytic processes. The comprehensive exploration of theoretical modeling approaches presented in this review serves as a valuable guide for researchers seeking to develop efficient catalysts for various electrochemical reactions. We believe that this expanded focus will attract more researchers to the field and promote innovation and progress in the development of sustainable catalytic technologies for a range of applications. By emphasizing these broader applications, we hope to stimulate research interest and accelerate progress in a wider range of electrocatalytic reduction reactions that are critical for renewable energy, environmental remediation and chemical synthesis.

Machine learning was briefly discussed as a method to improve catalyst design, as it offers higher efficiency and lower computational costs. The synergistic contribution of artificial intelligence, especially machine learning, in the field of multiscale eCO_2RR modeling should be emphasized more. Furthermore, there is a general lack of sensitivity analysis in the field of eCO_2RR multiscale modeling. Sensitivity analysis, an important tool in multiscale modeling, identifies the impact of uncertainty of a model input or a group of inputs on the model response.

Therefore, this area can also be considered for future research perspectives and further investigations.

Although there is an abundance of computational studies on CO_2RR, multiscale modeling has been mainly limited to thermocatalytic processes. This is mainly due to the historical emphasis on thermocatalysis as the driving force behind CO_2RR, the complexity and high computational cost of electrochemical systems, and the lack of experimental data for eCO_2RR. However, with the increasing focus on sustainable energy and advances in electrochemical technologies, there is a gradual shift towards eCO_2RR. In this review, we have focused exclusively on eCO_2RR, highlighting the significant advances and challenges in this particular area. While thermocatalytic CO_2 reduction has its own merits and has been extensively reviewed in several studies, our aim was to provide a detailed overview of electrochemical processes and their modeling techniques. We encourage readers interested in thermocatalytic approaches to refer to the comprehensive reviews available in this field. To change the direction of research towards electrochemical reduction, a multifaceted approach is required. By providing sufficient funding and support, fostering interdisciplinary and academic-industrial collaborations, encouraging experimenters to focus on eCO_2RR for experimental validation, promoting methodological advances and establishing data exchange, all these efforts can make an important contribution.

Nomenclature

AI	Artificial Intelligence
AIMD	ab initio molecular dynamics
CORR	CO Reduction Reaction
CO2RR	CO2 Reduction Reaction
CEP	Constant Electrode Potential
CFD	Computational Fluid Dynamics
CHE	Computational Hydrogen Electrode
DFT	Density Functional Theory
eCO_2RR	Electrochemical CO_2 Reduction Reaction
EP	Electrostatic Potential
FE	Faradaic Efficiency
FVM	Finite Volume Method
GPAW	Grid Projector Augmented Wave
HF	Hartree-Fock
HER	Hydrogen Evolution Reaction
KMC	Kinetic Monte Carlo
KS	Kohn-Sham
LPB-PCM	Linearized Poisson-Boltzmann/Polarizable Continuum Model
ML	Machine Learning
MFA	Mean-Feld Approximation
MEA	Membrane Electrode Assembly
MEOM	Metal Embedded in an Oxidized Matrix
MOF	Metal Organic Framework
MD	Molecular Dynamics
OER	Oxygen Evolution Reaction
PCET	Proton-Coupled Electron Transfer
PDOS	Projected Density of States
PES	Potential Energy Surface
QM	Quantum Mechanics
RDS	Rate-Determining Step
RHE	Reversible Hydrogen Electrode
SHE	Standard Hydrogen Electrode
SJM	Solvated Jellium Method
TOF	Turnover Frequency
TS	Transition State
TST	Transition-State Theory
WE	Working Electrode

Acknowledgments

We gratefully acknowledge the funding from the EU commission for Horizon 2020 Framework Programme-Marie Skłodowska-Curie Actions (MSCA) Individual Fellowships (IF), Project-CO2Polymerisation (Grant agreement 892003). The Slovenian Research and Innovation Agency (ARIS) is thanked for providing the infrastructure funding (I0-0039), core funding support (P2-0152) and project funding (J1-3020 – M.P., N1-0303 – M.H., J2-4424 – R.G., J7-4638 – B.L.). This research was partially funded by the HyBreed project by ARIS.

Conflict of Interests

The authors declare no conflict of interest.

Data Availability Statement

The data that support the findings of this study are available from the corresponding author upon reasonable request.

Keywords: Multiscale modeling · Molecular dynamics · Kinetic Monte Carlo · Computational fluid dynamics · Machine learning

[1] P. Friedlingstein, M. O'Sullivan, M. W. Jones, et al, *Earth Syst. Sci. Data.* **2023**, *15*(12), 5301–5369.
[2] Scripps Institution of Oceanography, US National Oceanic and Atmospheric Administration (NOAA), Trends in Atmospheric Carbon Dioxide, https://keelingcurve.ucsd.edu/ **2023**.
[3] C. Nullis, WMO Confirms That 2023 Smashes Global Temperature Record, https://wmo.int/news/media-centre/wmo-confirms-2023-smashes-global-temperature-record **2024**.
[4] S. O'Neill, *Engineering (Beijing)*. **2020**, *6*(9), 958–959.
[5] Y. Wang, C. Niu, D. Wang, *J. Colloid Interface Sci.* **2018**, *527*, 95–106.
[6] P. W. Atkins, J. De Paula, *Atkins' Physical Chemistry*, 8th ed., Oxford University Press, Oxford, New York **2006**.
[7] O. Martin, A. J. Martín, C. Mondelli, S. Mitchell, T. F. Segawa, R. Hauert, C. Drouilly, D. Curulla-Ferré, J. Pérez-Ramírez, *Angew. Chem. Int. Ed.* **2016**, *55*(21), 6261–6265.
[8] C. Liu, J. J. Gallagher, K. K. Sakimoto, E. M. Nichols, C. J. Chang, M. C. Y. Chang, P. Yang, *Nano Lett.* **2015**, *15*(5), 3634–3639.
[9] M. Mondal, S. Khanra, O. N. Tiwari, K. Gayen, G. N. Halder, *Environ. Prog. Sustain. Energy* **2016**, *35*(6), 1605–1615.
[10] J. Highfield, H. Lim, J. Fagerlund, R. Zevenhoven, *RSC Adv.* **2012**, *2*(16), 6535–6541.
[11] J. Gottschalk, L. C. Skinner, J. Lippold, H. Vogel, N. Frank, S. L. Jaccard, C. Waelbroeck, *Nat. Commun.* **2016**, *7*(1), 11539.

[12] M. Schreier, J. Luo, P. Gao, T. Moehl, M. T. Mayer, M. Grätzel, *J Am. Chem. Soc.* **2016**, *138*(6), 1938–1946.
[13] S. E. Renfrew, D. E. Starr, P. Strasser, *ACS Catal.* **2020**, *10*(21), 13058–13074.
[14] P. A. Alaba, A. Abbas, W. M. W. Daud, *J. Clean Prod.* **2017**, *140*, 1298–1312.
[15] M. Götz, J. Lefebvre, F. Mörs, A. McDaniel Koch, F. Graf, S. Bajohr, R. Reimert, T. Kolb, *Renew. Energy* **2016**, *85*, 1371–1390.
[16] A. Wuttig, C. Liu, Q. Peng, M. Yaguchi, C. H. Hendon, K. Motobayashi, S. Ye, M. Osawa, Y. Surendranath, *ACS Cent. Sci.* **2016**, *2*(8), 522–528.
[17] Y. Y. Birdja, E. Pérez-Gallent, M. C. Figueiredo, A. J. Göttle, F. Calle-Vallejo, M. T. M. Koper, *Nat. Energy.* **2019**, *4*(9), 732–745.
[18] L. Wang, S. A. Nitopi, E. Bertheussen, M. Orazov, C. G. Morales-Guio, X. Liu, D. C. Higgins, K. Chan, J. K. Nørskov, C. Hahn, et al., *ACS Catal.* **2018**, *8*(8), 7445–7454.
[19] X. Zhang, S. X. Guo, K. A. Gandionco, A. M. Bond, J. Zhang, *Mater. Today Adv.* **2020**, *7*, 100074.
[20] M. G. Kibria, J. P. Edwards, C. M. Gabardo, C. T. Dinh, A. Seifitokaldani, D. Sinton, E. H. Sargent, *Adv. Mater.* **2019**, *31*(31), 1–24.
[21] Z. W. She, J. Kibsgaard, C. F. Dickens, I. Chorkendorff, J. K. Nørskov, T. F. Jaramillo, *Science (1979)* **2017**, *355*(6321), eaad4998.
[22] A. Bagger, W. Ju, A. S. Varela, P. Strasser, J. Rossmeisl, *ChemPhysChem* **2017**, *18*(22), 3266–3273.
[23] A. Klinkova, P. De Luna, C.-T. Dinh, O. Voznyy, E. M. Larin, E. Kumacheva, E. H. Sargent, *ACS Catal.* **2016**, *6*(12), 8115–8120.
[24] M. Fan, S. Garbarino, G. A. Botton, A. C. Tavares, D. Guay, *J. Mater. Chem. A Mater.* **2017**, *5*(39), 20747–20756.
[25] C.-T. Dinh, F. P. García de Arquer, D. Sinton, E. H. Sargent, *ACS Energy Lett.* **2018**, *3*(11), 2835–2840.
[26] C. M. Gabardo, A. Seifitokaldani, J. P. Edwards, C.-T. Dinh, T. Burdyny, M. G. Kibria, C. P. O'Brien, E. H. Sargent, D. Sinton, *Energy Environ. Sci.* **2018**, *11*(9), 2531–2539.
[27] S. Verma, Y. Hamasaki, C. Kim, W. Huang, S. Lu, H.-R. M. Jhong, A. A. Gewirth, T. Fujigaya, N. Nakashima, P. J. A. Kenis, *ACS Energy Lett.* **2018**, *3*(1), 193–198.
[28] G. de A. F. Pelayo, D. Cao-Thang, O. Adnan, W. Joshua, M. Christopher, K. A. R. N. Dae-Hyun, G. Christine, S. Ali, W. Xue, et al., *Science (1979)* **2020**, *367*(6478), 661–666.
[29] J. J. Lv, M. Jouny, W. Luc, W. Zhu, J. J. Zhu, F. Jiao, *Adv. Mater.* **2018**, *30*(49), 1–8.
[30] K. P. Kuhl, E. R. Cave, D. N. Abram, T. F. Jaramillo, *Energy Environ Sci.* **2012**, *5*(5), 7050–7059.
[31] Y. Hori, H. Wakebe, T. Tsukamoto, O. Koga, *Electrochim Acta.* **1994**, *39*(11), 1833–1839.
[32] H. R. M. Jhong, S. Ma, P. J. Kenis, *Curr. Opin. Chem. Eng.* **2013**, *2*(2), 191–199.
[33] M. Ma, K. Djanashvili, W. A. Smith, *Angew. Chem. Int. Ed.* **2016**, *55*(23), 6680–6684.
[34] Z. Chen, G. Zhang, H. Chen, J. Prakash, Y. Zheng, S. Sun, *Renew. Sustain. Energy Rev.* **2022**, *155*, 111922.
[35] S. Nitopi, E. Bertheussen, S. B. Scott, X. Liu, A. K. Engstfeld, S. Horch, B. Seger, I. E. L. Stephens, K. Chan, C. Hahn, et al., *Chem. Rev.* **2019**, *119*(12), 7610–7672.
[36] Y. Hori, R. Takahashi, Y. Yoshinami, A. Murata, *J. Phys. Chem. B* **1997**, *101*(36), 7075–7081.
[37] A. A. Peterson, F. Abild-Pedersen, F. Studt, J. Rossmeisl, J. K. Nørskov, *Energy Environ. Sci.* **2010**, *3*(9), 1311–1315.
[38] J. H. Montoya, C. Shi, K. Chan, J. K. Nørskov, *J Phys Chem Lett.* **2015**, *6*(11), 2032–2037.
[39] R. Kortlever, J. Shen, K. J. P. Schouten, F. Calle-Vallejo, M. T. M. Koper, *J. Phys. Chem. Lett.* **2015**, *6*(20), 4073–4082.
[40] T. Cheng, H. Xiao, W. A. Goddard, *J. Phys. Chem. Lett.* **2015**, *6*(23), 4767–4773.
[41] Y. Lum, T. Cheng, W. A. Goddard, J. W. Ager, *J. Am. Chem. Soc.* **2018**, *140*(30), 9337–9340.
[42] J. T. Feaster, C. Shi, E. R. Cave, T. Hatsukade, D. N. Abram, K. P. Kuhl, C. Hahn, J. K. Nørskov, T. F. Jaramillo, *ACS Catal.* **2017**, *7*(7), 4822–4827.
[43] X. Liu, P. Schlexer, J. Xiao, Y. Ji, L. Wang, R. B. Sandberg, M. Tang, K. S. Brown, H. Peng, S. Ringe, et al., *Nat. Commun.* **2019**, *10*(1), 32.
[44] A. J. Garza, A. T. Bell, M. Head-Gordon, *ACS Catal.* **2018**, *8*(2), 1490–1499.
[45] E. Gileadi, *Electrode Kinetics for Chemists, Chemical Engineers, and Materials Scientists*, John Wiley and Sons, Hoboken, NJ **1993**.
[46] C. W. Lee, N. H. Cho, S. W. Im, M. S. Jee, Y. J. Hwang, B. K. Min, K. T. Nam, *J. Mater. Chem. A Mater.* **2018**, *6*(29), 14043–14057.
[47] C. Oloman, H. Li, *ChemSusChem* **2008**, *1*(5), 385–391.
[48] F. Calle-Vallejo, M. T. M. Koper, *Angew. Chem. Int. Ed.* **2013**, *52*(28), 7282–7285.
[49] T. K. Todorova, M. W. Schreiber, M. Fontecave, *ACS Catal.* **2020**, *10*(3), 1754–1768.
[50] A. Vasileff, C. Xu, Y. Jiao, Y. Zheng, S.-Z. Qiao, *Chem* **2018**, *4*(8), 1809–1831.
[51] N. Han, P. Ding, L. He, Y. Li, Y. Li, *Adv Energy Mater.* **2020**, *10*(11), 1902338.
[52] K. Jan Schouten, M. Koper, *RSC Energy Environ. Ser.* **2013**, 333–358.
[53] H. Zhang, J. Li, M.-J. Cheng, Q. Lu, *ACS Catal.* **2019**, *9*(1), 49–65.
[54] Z. W. Seh, J. Kibsgaard, C. F. Dickens, I. Chorkendorff, J. K. Nørskov, T. F. Jaramillo, *Science (1979)*. **2017**, *355*(6321), eaad4998.
[55] G. M. Tomboc, S. Choi, T. Kwon, Y. J. Hwang, K. Lee, *Adv. Mater.* **2020**, *32*(17), 1908398.
[56] W. Luo, X. Nie, M. J. Janik, A. Asthagiri, *ACS Catal.* **2016**, *6*(1), 219–229.
[57] Y. Zheng, A. Vasileff, X. Zhou, Y. Jiao, M. Jaroniec, S. Z. Qiao, *J. Am. Chem. Soc.* **2019**, *141*(19), 7646–7659.
[58] Y. Cheng, S. Yang, S. P. Jiang, S. Wang, *Small Methods* **2019**, *3*(9), 1800440.
[59] F. Lei, X. Chuan, Y. Fangqi, W. Jun, W. Haotian, L. Yingying, *Sci. Adv.* **2022**, *6*(8), eaay3111.
[60] C. Jia, K. Dastafkan, W. Ren, W. Yang, C. Zhao, *Sustain. Energy Fuels* **2019**, *3*(11), 2890–2906.
[61] D. D. Zhu, J. L. Liu, S. Z. Qiao, *Adv. Mater.* **2016**, *28*(18), 3423–3452.
[62] N. Elgrishi, *Electrochemical Reduction of CO2 to Fuels by Molecular Polypyridyl Catalysts of 3D Transition Metals*, Université Pierre Et Marie Curie, Paris VI **2015**.
[63] Q. Fan, M. Zhang, M. Jia, S. Liu, J. Qiu, Z. Sun, *Mater Today Energy* **2018**, *10*, 280–301.
[64] Z. Sun, T. Ma, H. Tao, Q. Fan, B. Han, *Chem.* **2017**, *3*(4), 560–587.
[65] C. Costentin, M. Robert, J.-M. Savéant, *Chem. Soc. Rev.* **2013**, *42*(6), 2423–2436.
[66] F. Yu, K. Deng, M. Du, W. Wang, F. Liu, D. Liang, *Carbon Capture Sci. Technol.* **2023**, *6*, 100081.
[67] Q. Chen, P. Tsiakaras, P. Shen, *Catalysts.* **2022**, *12*(11), 1348.
[68] Y. Chen, M. W. Kanan, *J. Am. Chem. Soc.* **2012**, *134*(4), 1986–1989.
[69] R. Hinogami, S. Yotsuhashi, M. Deguchi, Y. Zenitani, H. Hashiba, Y. Yamada, *ECS Electrochem. Lett.* **2012**, *1*(4), H17–H19.
[70] C. W. Li, M. W. Kanan, *J. Am. Chem. Soc.* **2012**, *134*(17), 7231–7234.
[71] W. Ma, S. Xie, T. Liu, Q. Fan, J. Ye, F. Sun, Z. Jiang, Q. Zhang, J. Cheng, Y. Wang, *Nat. Catal.* **2020**, *3*(6), 478–487.
[72] L. Zhang, Z. J. Zhao, J. Gong, *Angew. Chem. Int. Ed.* **2017**, *56*(38), 11326–11353.
[73] Q. Lu, J. Rosen, F. Jiao, *ChemCatChem* **2015**, *7*(1), 38–47.
[74] J. Liu, C. Guo, A. Vasileff, S. Qiao, *Small Methods* **2017**, *1*(1–2), 1600006.
[75] A. Wuttig, Y. Surendranath, *ACS Catal.* **2015**, *5*(7), 4479–4484.
[76] C. Zhang, S. Yang, J. Wu, M. Liu, S. Yazdi, M. Ren, J. Sha, J. Zhong, K. Nie, A. S. Jalilov, et al., *Adv. Energy Mater.* **2018**, *8*(19), 1703487.
[77] M. C. Figueiredo, I. Ledezma-Yanez, M. T. M. Koper, *ACS Catal.* **2016**, *6*(4), 2382–2392.
[78] R. Wang, X. Sun, S. Ould-Chikh, D. Osadchii, F. Bai, F. Kapteijn, J. Gascon, *ACS Appl. Mater. Interfaces* **2018**, *10*(17), 14751–14758.
[79] J. Wu, M. Liu, P. P. Sharma, R. M. Yadav, L. Ma, Y. Yang, X. Zou, X.-D. Zhou, R. Vajtai, B. I. Yakobson, et al., *Nano Lett.* **2016**, *16*(1), 466–470.
[80] W. Bi, X. Li, R. You, M. Chen, R. Yuan, W. Huang, X. Wu, W. Chu, C. Wu, Y. Xie, *Adv. Mater.* **2018**, *30*(18), 1706617.
[81] H. R. M. Jhong, C. E. Tornow, B. Smid, A. A. Gewirth, S. M. Lyth, P. J. A. Kenis, *ChemSusChem* **2017**, *10*(6), 1094–1099.
[82] M. Zhu, J. Chen, L. Huang, R. Ye, J. Xu, Y. F. Han, *Angew. Chem. Int. Ed.* **2019**, *58*(20), 6595–6599.
[83] J. Wu, R. M. Yadav, M. Liu, P. P. Sharma, C. S. Tiwary, L. Ma, X. Zou, X.-D. Zhou, B. I. Yakobson, J. Lou, et al., *ACS Nano* **2015**, *9*(5), 5364–5371.
[84] J. Xie, X. Zhao, M. Wu, Q. Li, Y. Wang, J. Yao, *Angew. Chem. Int. Ed.* **2018**, *57*(31), 9640–9644.
[85] C. Zhao, X. Dai, T. Yao, W. Chen, X. Wang, J. Wang, J. Yang, S. Wei, Y. Wu, Y. Li, *J. Am. Chem. Soc.* **2017**, *139*(24), 8078–8081.
[86] X. Wang, Z. Chen, X. Zhao, T. Yao, W. Chen, R. You, C. Zhao, G. Wu, J. Wang, W. Huang, et al., *Angew. Chem. Int. Ed.* **2018**, *57*(7), 1944–1948.
[87] W. Ren, X. Tan, W. Yang, C. Jia, S. Xu, K. Wang, S. C. Smith, C. Zhao, *Angew. Chem. Int. Ed.* **2019**, *58*(21), 6972–6976.
[88] P. Lu, Y. Yang, J. Yao, M. Wang, S. Dipazir, M. Yuan, J. Zhang, X. Wang, Z. Xie, G. Zhang, *Appl. Catal. B* **2019**, *241*, 113–119.
[89] Y. Zhao, J. Liang, C. Wang, J. Ma, G. G. Wallace, *Adv. Energy Mater.* **2018**, *8*(10), 1702524.

[90] S. Liu, H. Yang, X. Huang, L. Liu, W. Cai, J. Gao, X. Li, T. Zhang, Y. Huang, B. Liu, *Adv. Funct. Mater.* **2018**, *28*(21), 1800499.
[91] Y. Pan, R. Lin, Y. Chen, S. Liu, W. Zhu, X. Cao, W. Chen, K. Wu, W.-C. Cheong, Y. Wang, et al., *J. Am. Chem. Soc.* **2018**, *140*(12), 4218–4221.
[92] N. Leonard, W. Ju, I. Sinev, J. Steinberg, F. Luo, A. S. Varela, B. Roldan Cuenya, P. Strasser, *Chem. Sci.* **2018**, *9*(22), 5064–5073.
[93] M. Ma, K. Djanashvili, W. A. Smith, *Phys. Chem. Chem. Phys.* **2015**, *17*(32), 20861–20867.
[94] C. Wang, M. Cao, X. Jiang, M. Wang, Y. Shen, *Electrochim. Acta* **2018**, *271*, 544–550.
[95] M. Tiwari, S. C. Mandal, A. Das, B. Pathak, *ACS Appl. Nano Mater.* **2023**, *6*(9), 7156–7165.
[96] W. Quan, Y. Lin, Y. Luo, Y. Huang, *Adv. Sci. (Weinh)* **2021**, *8*(23), 2101597.
[97] A. G. Nabi, A. Ur-Rehman, A. Hussain, G. Chass, D. Di Tommaso, *Nanomaterials (Basel)* **2023**, *13*, 87.
[98] S. Ma, M. Sadakiyo, M. Heima, R. Luo, R. T. Haasch, J. I. Gold, M. Yamauchi, P. J. A. Kenis, *J. Am. Chem. Soc.* **2017**, *139*(1), 47–50.
[99] W. Luc, C. Collins, S. Wang, H. Xin, K. He, Y. Kang, F. Jiao, *J. Am. Chem. Soc.* **2017**, *139*(5), 1885–1893.
[100] H. Yang, J. J. Kaczur, S. D. Sajjad, R. I. Masel, *J. CO2 Util.* **2017**, *20*, 208–217.
[101] Y. Mi, S. Shen, X. Peng, H. Bao, X. Liu, J. Luo, *ChemElectroChem* **2019**, *6*(9), 2393–2397.
[102] T. T. H. Hoang, S. Verma, S. Ma, T. T. Fister, J. Timoshenko, A. I. Frenkel, P. J. A. Kenis, A. A. Gewirth, *J. Am. Chem. Soc.* **2018**, *140*(17), 5791–5797.
[103] L. Zaza, K. Rossi, R. Buonsanti, *ACS Energy Lett.* **2022**, *7*(4), 1284–1291.
[104] X.-Q. Wang, Q. Chen, Y.-J. Zhou, H.-M. Li, J.-W. Fu, M. Liu, *Adv. Sens. Energy Mater.* **2022**, *1*(3), 100023.
[105] C. Chen, Y. Li, S. Yu, S. Louisia, J. Jin, M. Li, M. B. Ross, P. Yang, *Joule.* **2020**, *4*(8), 1688–1699.
[106] M. Xing, L. Guo, Z. Hao, *Dalton Trans.* **2019**, *48*(4), 1504–1515.
[107] L. Han, H. Liu, P. Cui, Z. Peng, S. Zhang, J. Yang, *Sci. Rep.* **2014**, *4*(1), 6414.
[108] H. S. Jeon, J. Timoshenko, F. Scholten, I. Sinev, A. Herzog, F. T. Haase, B. Roldan Cuenya, *J. Am. Chem. Soc.* **2019**, *141*(50), 19879–19887.
[109] Y. Deng, Y. Huang, D. Ren, A. D. Handoko, Z. W. Seh, P. Hirunsit, B. S. Yeo, *ACS Appl. Mater. Interfaces* **2018**, *10*(34), 28572–28581.
[110] K. Ye, A. Cao, J. Shao, G. Wang, R. Si, N. Ta, J. Xiao, G. Wang, *Sci. Bull (Beijing).* **2020**, *65*(9), 711–719.
[111] S. Sarfraz, A. T. Garcia-Esparza, A. Jedidi, L. Cavallo, K. Takanabe, *ACS Catal.* **2016**, *6*(5), 2842–2851.
[112] J. Zeng, K. Bejtka, W. Ju, M. Castellino, A. Chiodoni, A. Sacco, M. A. Farkhondehfal, S. Hernández, D. Rentsch, C. Battaglia, et al., *Appl. Catal. B* **2018**, *236*, 475–482.
[113] J. Feng, L. Wu, S. Liu, L. Xu, X. Song, L. Zhang, Q. Zhu, X. Kang, X. Sun, B. Han, *J. Am. Chem. Soc.* **2023**, *145*(17), 9857–9866.
[114] X. Chen, D. A. Henckel, U. O. Nwabara, Y. Li, A. I. Frenkel, T. T. Fister, P. J. A. Kenis, A. A. Gewirth, *ACS Catal.* **2020**, *10*(1), 672–682.
[115] D. Ren, J. Fong, B. S. Yeo, *Nat. Commun.* **2018**, *9*(1), 925.
[116] J. M. Spurgeon, B. Kumar, *Energy Environ. Sci.* **2018**, *11*(6), 1536–1551.
[117] M. Jouny, W. Luc, F. Jiao, *Ind. Eng. Chem. Res.* **2018**, *57*(6), 2165–2177.
[118] O. S. Bushuyev, P. De Luna, C. T. Dinh, L. Tao, G. Saur, J. van de Lagemaat, S. O. Kelley, E. H. Sargent, *Joule* **2018**, *2*(5), 825–832.
[119] C. W. Li, J. Ciston, M. W. Kanan, *Nature* **2014**, *508*(7497), 504–507.
[120] A. S. Agarwal, Y. Zhai, D. Hill, N. Sridhar, *ChemSusChem* **2011**, *4*(9), 1301–1310.
[121] M. Gangeri, S. Perathoner, S. Caudo, G. Centi, J. Amadou, D. Bégin, C. Pham-Huu, M. J. Ledoux, J.-P. Tessonnier, D. S. Su, et al., *Catal. Today* **2009**, *143*(1), 57–63.
[122] S. A. Akhade, W. Luo, X. Nie, N. J. Bernstein, A. Asthagiri, M. J. Janik, *Phys. Chem. Chem. Phys.* **2014**, *16*(38), 20429–20435.
[123] G. Ma, O. A. Syzgantseva, Y. Huang, D. Stoian, J. Zhang, S. Yang, W. Luo, M. Jiang, S. Li, C. Chen, et al., *Nat. Commun.* **2023**, *14*(1), 501.
[124] Y.-J. Zhang, V. Sethuraman, R. Michalsky, A. A. Peterson, *ACS Catal.* **2014**, *4*(10), 3742–3748.
[125] G. Liu, T. Tran-Phu, H. Chen, A. Tricoli, *Adv. Sustain. Syst.* **2018**, *2*(8–9), 1–13.
[126] X. She, Y. Wang, H. Xu, S. Chi Edman Tsang, S. Ping Lau, *Angew. Chem. Int. Ed.* **2022**, *61*(49), e202211396.
[127] S. Jin, Z. Hao, K. Zhang, Z. Yan, J. Chen, *Angew. Chem. Int. Ed.* **2021**, *60*(38), 20627–20648.
[128] T. Mou, X. Han, H. Zhu, H. Xin, *Curr. Opin. Chem. Eng.* **2022**, *36*, 100825.
[129] L. Qi, S. Liu, W. Gao, Q. Jiang, *J. Phys. Chem. C* **2018**, *122*(10), 5472–5480.
[130] M. Salciccioli, M. Stamatakis, S. Caratzoulas, D. G. Vlachos, *Chem. Eng. Sci.* **2011**, *66*(19), 4319–4355.
[131] Z. P. Jovanov, H. A. Hansen, A. S. Varela, P. Malacrida, A. A. Peterson, J. K. Nørskov, I. E. L. Stephens, I. Chorkendorff, *J. Catal.* **2016**, *343*, 215–231.
[132] M. R. Singh, J. D. Goodpaster, A. Z. Weber, M. Head-Gordon, A. T. Bell, *Proc. Natl. Acad. Sci. U.S.A.* **2017**, *114*(42), E8812–E8821.
[133] Z. Masood, Q. Ge, *Molecules* **2023**, *28*(1), 375.
[134] Q. Lu, F. Jiao, *Nano Energy* **2016**, *29*, 439–456.
[135] B. E. Rapp, *Micro and Nano Technologies* (Ed: B. E. B. T.-M. Second, E. Rapp), Elsevier **2023**.
[136] J. Hou, B. Xu, Q. Lu, *Nat. Commun.* **2024**, *15*(1), 1926.
[137] P. Li, Y. Jiao, J. Huang, S. Chen, *JACS Au.* **2023**, *3*(10), 2640–2659.
[138] C. K. Li, J. Zhang, J. Huang, *J. Chem. Phys.* **2022**, *157*(18), 184704.
[139] S. J. Shin, D. H. Kim, G. Bae, S. Ringe, H. Choi, H. K. Lim, C. H. Choi, H. Kim, *Nat. Commun.* **2022**, *13*(1), 174.
[140] J. Huang, *J. Electroanal. Chem.* **2020**, *870*, 114243.
[141] S. Xu, E. A. Carter, *Chem. Rev.* **2019**, *119*(11), 6631–6669.
[142] S. Nitopi, E. Bertheussen, S. B. Scott, X. Liu, A. K. Engstfeld, S. Horch, B. Seger, I. E. L. Stephens, K. Chan, C. Hahn, et al., *Chem Rev.* **2019**, *119*(12), 7610–7672.
[143] J. K. Nørskov, J. Rossmeisl, A. Logadottir, L. Lindqvist, J. R. Kitchin, T. Bligaard, H. Jónsson, *J. Phys. Chem. B* **2004**, *108*(46), 17886–17892.
[144] J. D. Goodpaster, A. T. Bell, M. Head-Gordon, *J. Phys. Chem. Lett.* **2016**, *7*(8), 1471–1477.
[145] R. Jinnouchi, A. B. Anderson, *J. Phys. Chem. C* **2008**, *112*(24), 8747–8750.
[146] R. Jinnouchi, A. B. Anderson, *Phys. Rev. B* **2008**, *77*(24), 245417.
[147] W. A. Donald, R. D. Leib, J. T. O'Brien, M. F. Bush, E. R. Williams, *J. Am. Chem. Soc.* **2008**, *130*(11), 3371–3381.
[148] G. Kastlunger, P. Lindgren, A. A. Peterson, *J. Phys. Chem. C* **2018**, *122*(24), 12771–12781.
[149] A. Held, M. Walter, *J. Chem. Phys.* **2014**, *141*(17), 174108.
[150] K. Mathew, R. Sundararaman, K. Letchworth-Weaver, T. A. Arias, R. G. Hennig, *J. Chem. Phys.* **2014**, *140*(8), 84106.
[151] S. Ringe, H. Oberhofer, C. Hille, S. Matera, K. Reuter, *J Chem Theory Comput.* **2016**, *12*(8), 4052–4066.
[152] R. Sundararaman, K. Schwarz, *J. Chem. Phys.* **2017**, *146*(8), 84111.
[153] J. A. Gauthier, S. Ringe, C. F. Dickens, A. J. Garza, A. T. Bell, M. Head-Gordon, J. K. Nørskov, K. Chan, *ACS Catal.* **2019**, *9*(2), 920–931.
[154] H. Xiao, T. Cheng, W. A. I. I. I. Goddard, R. Sundararaman, *J Am Chem Soc.* **2016**, *138*(2), 483–486.
[155] T. Ludwig, J. A. Gauthier, K. S. Brown, S. Ringe, J. K. Nørskov, K. Chan, *J. Phys. Chem. C* **2019**, *123*(10), 5999–6009.
[156] Z. Zhao, G. Lu, *J. Phys. Chem. C* **2019**, *123*(7), 4380–4387.
[157] A. Klamt, *WIREs Comput. Mol. Sci.* **2018**, *8*(1), e1338.
[158] A. Rendón-Calle, S. Builes, F. Calle-Vallejo, *Appl. Catal. B* **2020**, *276*, 119147.
[159] S.-Q. Xiang, S. T. Gao, J. L. Shi, W. Zhang, L. B. Zhao, *J. Catal.* **2021**, *393*, 11–19.
[160] M. Stamatakis, D. G. Vlachos, *ACS Catal.* **2012**, *2*(12), 2648–2663.
[161] M. Stamatakis, S. Piccinin, *ACS Catal.* **2016**, *6*(3), 2105–2111.
[162] S. Matera, M. Maestri, A. Cuoci, K. Reuter, *ACS Catal.* **2014**, *4*(11), 4081–4092.
[163] L. Monticelli, D. P. Tieleman, *Biomolecular Simulations: Methods and Protocols* (Eds: L. Monticelli, E. Salonen), Humana Press, Totowa, NJ **2013**.
[164] Q. Mao, M. Feng, X. Z. Jiang, Y. Ren, K. H. Luo, A. C. T. van Duin, *Prog. Energy Combust. Sci.* **2023**, *97*, 101084.
[165] T. P. Senftle, S. Hong, M. M. Islam, S. B. Kylasa, Y. Zheng, Y. K. Shin, C. Junkermeier, R. Engel-Herbert, M. J. Janik, H. M. Aktulga, et al., *NPJ Comput Mater.* **2016**, *2*(1), 15011.
[166] T. Liang, Y. T. Cheng, X. Nie, W. Luo, A. Asthagiri, M. J. Janik, E. Andrews, J. Flake, S. B. Sinnott, *Catal. Commun.* **2014**, *52*, 84–87.
[167] D. Loco, L. Lagardère, S. Caprasecca, F. Lipparini, B. Mennucci, J. P. Piquemal, *J. Chem. Theory Comput.* **2017**, *13*(9), 4025–4033.
[168] D. Bedrov, J. P. Piquemal, O. Borodin, A. D. Jr. MacKerell, B. Roux, C. Schröder, *Chem. Rev.* **2019**, *119*(13), 7940–7995.
[169] S. Liu, R. Dupuis, D. Fan, S. Benzaria, M. Bonneau, P. Bhatt, M. Eddaoudi, G. Maurin, *Chem. Sci.* **2024**, *15*(14), 5294–5302.
[170] B. Kim, Y. C. Tan, Y. Ryu, K. Jang, H. G. Abbas, T. Kang, H. Choi, K.-S. Lee, S. Park, W. Kim, et al., *ACS Energy Lett.* **2023**, *8*(8), 3356–3364.

[171] L. R. L. Ting, O. Piqué, S. Y. Lim, M. Tanhaei, F. Calle-Vallejo, B. S. Yeo, *ACS Catal.* **2020**, *10*(7), 4059–4069.
[172] S. C. Mandal, K. S. Rawat, P. Garg, B. Pathak, *ACS Appl. Nano Mater.* **2019**, *12*, 7686–7695.
[173] W. Luo, W. Xie, R. Mutschler, E. Oveisi, G. L. De Gregorio, R. Buonsanti, A. Züttel, *ACS Catal.* **2018**, *8*(7), 6571–6581.
[174] T. Cheng, H. Xiao, W. A. Goddard, *J. Am. Chem. Soc.* **2016**, *138*(42), 13802–13805.
[175] J. Santatiwongchai, K. Faungnawakij, P. Hirunsit, *ACS Catal.* **2021**, *11*(15), 9688–9701.
[176] X. Meng, G. Pan, H. Liu, Y. Qian, X. Wang, C. Wang, L. Hu, H. Wang, Q. Chen, *ACS Appl. Mater. Interfaces* **2022**, *14*(15), 17240–17248.
[177] T. Liu, G. Song, X. Liu, Z. Chen, Y. Shen, Q. Wang, Z. Peng, G. Wang, *iScience* **2023**, *26*(10), 107953.
[178] C. Soulaine, S. Pavuluri, F. Claret, C. Tournassat, *Environ. Modell. Softw.* **2021**, *145*, 105199.
[179] I. Alekseev, E. Kustova, *Phys. Fluids (1994)* **2021**, *33*(9), 96101.
[180] P. G. Robert, J. Kee, M. E. Coltrin, *Chemically Reacting Flow: Theory and Practice*, John Wiley & Sons, Hoboken, NJ **2003**.
[181] M. Pérez-Fortes, J. Vos, T. Wiltink, I. van de Poel, H. de Bruijn, T. Tan, N. Mutlu, F. Alkemade, A. Ramirez Ramirez, *16th Greenhouse Gas Control Technologies Conference* (*GHGT-16*) **2022**.
[182] X. H. Yang, Y. B. Zhuang, J. X. Zhu, J. B. Le, J. Cheng, *WIREs Comput. Mol. Sci.* **2022**, *12*(1), e1559.
[183] Y. Wang, H. Shao, C. Zhang, F. Liu, J. Zhao, S. Zhu, M. K. H. Leung, J. Hu, *Energy Rev.* **2023**, *2*(3), 100028.
[184] K. S. Chavan, I. Matanovic, S. Calabrese Barton, *ECS Meet. Abstr.* **2018**, *MA2018–02(52)*, 1792.
[185] T. Sheng, S. G. Sun, *Chem. Commun.* **2017**, *53*(17), 2594–2597.
[186] A. Bruix, J. T. Margraf, M. Andersen, K. Reuter, *Nat. Catal.* **2019**, *2*(8), 659–670.
[187] J. Wang, S. Olsson, C. Wehmeyer, A. Pérez, N. E. Charron, G. de Fabritiis, F. Noé, C. Clementi, *ACS Cent. Sci.* **2019**, *5*(5), 755–767.
[188] Q. Xue, X. Qi, T. Yang, J. Jiang, Q. Zhou, C. Fu, N. Yang, *Nanomaterials (Basel)* **2022**, *12*(13), 2239.
[189] T. Liu, Q. Wang, G. Wang, X. Bao, *Green Chem.* **2021**, *23*(3), 1212–1219.
[190] H. Xu, D. Rebollar, H. He, L. Chong, Y. Liu, C. Liu, C.-J. Sun, T. Li, J. V Muntean, R. E. Winans, et al., *Nat. Energy.* **2020**, *5*(8), 623–632.
[191] S. Liang, L. Huang, Y. Gao, Q. Wang, B. Liu, *Adv. Sci. (Weinh)* **2021**, *8*(24), 2102886.
[192] X. Nie, W. Luo, M. J. Janik, A. Asthagiri, *J. Catal.* **2014**, *312*, 108–122.
[193] K. S. Rawat, A. Mahata, B. Pathak, *J. Catal.* **2017**, *349*, 118–127.
[194] P. Hirunsit, W. Soodsawang, J. Limtrakul, *J. Phys. Chem. C* **2015**, *119*(15), 8238–8249.
[195] Q. Zhao, E. A. Carter, *J. Chem. Theory Comput.* **2020**, *16*(10), 6528–6538.
[196] K. Jiang, R. B. Sandberg, A. J. Akey, X. Liu, D. C. Bell, J. K. Nørskov, K. Chan, H. Wang, *Nat. Catal.* **2018**, *1*(2), 111–119.
[197] H. Xiao, W. A. Goddard, T. Cheng, Y. Liu, *Proc. Natl. Acad. Sci.* **2017**, *114*(26), 6685–6688.
[198] X. Yuan, S. Chen, D. Cheng, L. Li, W. Zhu, D. Zhong, Z.-J. Zhao, J. Li, T. Wang, J. Gong, *Angew. Chem. Int. Ed.* **2021**, *60*(28), 15344–15347.
[199] I. V Chernyshova, P. Somasundaran, S. Ponnurangam, *Proc. Natl. Acad. Sci.* **2018**, *115*(40), E9261–E9270.
[200] S. A. Akhade, W. Luo, X. Nie, A. Asthagiri, M. J. Janik, *Catal. Sci. Technol.* **2016**, *6*(4), 1042–1053.
[201] T. Cheng, H. Xiao, W. A. Goddard, *Proc. Natl. Acad. Sci. U.S.A.* **2017**, *114*(8), 1795–1800.
[202] E. Pérez-Gallent, M. C. Figueiredo, F. Calle-Vallejo, M. T. M. Koper, *Angew. Chem. Int. Ed.* **2017**, *56*(13), 3621–3624.
[203] A. D. Handoko, K. W. Chan, B. S. Yeo, *ACS Energy Lett.* **2017**, *2*(9), 2103–2109.
[204] X. Nie, M. R. Esopi, M. J. Janik, A. Asthagiri, *Angew. Chem. Int. Ed.* **2013**, *52*(9), 2459–2462.
[205] G. Zhang, T. Wang, M. Zhang, L. Li, D. Cheng, S. Zhen, Y. Wang, J. Qin, Z.-J. Zhao, J. Gong, *Nat. Commun.* **2022**, *13*(1), 7768.
[206] M. Van den Bossche, C. Rose-Petruck, H. Jónsson, *J. Phys. Chem. C* **2021**, *125*(25), 13802–13808.
[207] Q. Chang, J. H. Lee, Y. Liu, Z. Xie, S. Hwang, N. S. Marinkovic, A. H. A. Park, S. Kattel, J. G. Chen, *JACS Au.* **2022**, *2*(1), 214–222.
[208] Q. Chang, J. H. Lee, Y. Liu, Z. Xie, S. Hwang, N. S. Marinkovic, A.-H. A. Park, S. Kattel, J. G. Chen, *JACS Au.* **2022**, *2*(1), 214–222.
[209] Y. He, P. Zelenay, *ECS Meet. Abstr.* **2022**, *MA2022–01(49)*, 2096.
[210] X. Wang, Q. Hu, G. Li, H. Yang, C. He, *Electrochem. Energy Rev.* **2022**, *5*(2), 28.
[211] M. Song, Z. Jiao, W. Jing, Y. Liu, L. Guo, *J. Phys. Chem. Lett.* **2022**, *13*(20), 4434–4440.
[212] C. Long, X. Liu, K. Wan, Y. Jiang, P. An, C. Yang, G. Wu, W. Wang, J. Guo, L. Li, et al., *Sci. Adv.* **2024**, *9*(43), eadi6119.
[213] O. V. D. K. F. H. C. I. S. P. P. et al. Plaza-Mayoral E, *ChemRxiv* **2024**.
[214] L. Ma, Z. Yang, Y. Wang, Y. Xia, *Adv Energy Sustain. Res.* **2023**, *4*(10), 2300034.
[215] S. Cui, S. Li, R. Deng, L. Wei, S. Yang, S. Dai, F. Wang, S. Liu, Y. Huang, *Catal. Sci. Technol.* **2024**, *14*, 2697.
[216] R. An, X. Chen, Q. Fang, Y. Meng, X. Li, Y. Cao, *Front. Chem.* **2023**, *11*, 1141453.
[217] Y. Chen, R. K. Miao, C. Yu, D. Sinton, K. Xie, E. H. Sargent, *Matter* **2024**, *7*(1), 25–37.
[218] Y. Qin, W. Zhao, C. Xia, L. J. Yu, F. Song, J. Zhang, T. Wu, R. Cao, S. Ding, Y. Su, et al., *Angew. Chem. Int. Ed.* **2024**, *n/a* (n/a), e202404763.
[219] W. Andreoni, S. Yip, *Handbook of Materials Modeling: Applications: Current and Emerging Materials*, Springer, Cham **2020**.
[220] M. Besora, F. Maseras, *WIREs Comput. Mol. Sci.* **2018**, *8*(6), e1372.
[221] D. Q. Liu, M. Kang, D. Perry, C. H. Chen, G. West, X. Xia, S. Chaudhuri, Z. P. L. Laker, N. R. Wilson, G. N. Meloni, et al., *Nat. Commun.* **2021**, *12*(1), 7110.
[222] J. Li, J. H. Stenlid, T. Ludwig, P. S. Lamoureux, F. Abild-Pedersen, *J. Am. Chem. Soc.* **2021**, *143*(46), 19341–19355.
[223] S. Vijay, W. Ju, S. Brückner, S.-C. Tsang, P. Strasser, K. Chan, *Nat. Catal.* **2021**, *4*(12), 1024–1031.
[224] G. Kastlunger, L. Wang, N. Govindarajan, H. H. Heenen, S. Ringe, T. Jaramillo, C. Hahn, K. Chan, *ACS Catal.* **2022**, *12*(8), 4344–4357.
[225] A. M. Limaye, J. S. Zeng, A. P. Willard, K. Manthiram, *Nat. Commun.* **2021**, *12*(1), 703.
[226] H. J. Peng, M. T. Tang, J. Halldin Stenlid, X. Liu, F. Abild-Pedersen, *Nat. Commun.* **2022**, *13*(1), 1399.
[227] J. Li, I. Maresi, Y. Lum, J. W. Ager, *J. Chem. Phys.* **2021**, *155*(16), 164701.
[228] Y. Feng, W. An, Z. Wang, Y. Wang, Y. Men, Y. Du, *ACS Sustain. Chem. Eng.* **2020**, *8*(1), 210–222.
[229] B. Zijlstra, X. Zhang, J. X. Liu, I. A. W. Filot, Z. Zhou, S. Sun, E. J. M. Hensen, *Electrochim. Acta* **2020**, *335*, 135665.
[230] A. Auer, M. Andersen, E.-M. Wernig, N. G. Hörmann, N. Buller, K. Reuter, J. Kunze-Liebhäuser, *Nat. Catal.* **2020**, *3*(10), 797–803.
[231] N. Liu, L. Chen, K. Deng, H. Feng, Y. Zhang, J. Duan, D. Liu, Q. Li, *Sci. Bull. (Beijing)*. **2023**, *68*(11), 1143–1152.
[232] N. Karmodak, S. Vijay, G. Kastlunger, K. Chan, *ACS Catal.* **2022**, *12*(9), 4818–4824.
[233] H. Peng, M. T. Tang, X. Liu, P. Schlexer Lamoureux, M. Bajdich, F. Abild-Pedersen, *Energy Environ. Sci.* **2021**, *14*(1), 473–482.
[234] Y. Hori, I. Takahashi, O. Koga, N. Hoshi, *J. Phys. Chem. B* **2002**, *106*(1), 15–17.
[235] Y. Hori, I. Takahashi, O. Koga, N. Hoshi, *J. Mol. Catal. A Chem.* **2003**, *199*(1–2), 39–47.
[236] K. Hara, A. Kudo, T. Sakata, *J. Electroanal. Chem.* **1995**, *391*(1), 141–147.
[237] X. Liu, J. Xiao, H. Peng, X. Hong, K. Chan, J. K. Nørskov, *Nat. Commun.* **2017**, *8*(1), 15438.
[238] X. Hou, Y. Cai, D. Zhang, L. Li, X. Zhang, Z. Zhu, L. Peng, Y. Liu, J. Qiao, *J. Mater. Chem. A Mater.* **2019**, *7*(7), 3197–3205.
[239] A. Rodríguez, F. F. Rivera, G. Orozco, G. Carreño, F. Castañeda, *Electrochim. Acta* **2018**, *282*, 520–532.
[240] L. Huang, D. Li, J. Liu, L. Yang, C. Dai, N. Ren, Y. Feng, *Chemosphere* **2021**, *262*, 127626.
[241] B. Jung, S. Park, C. Lim, W. H. Lee, Y. Lim, J. Na, C. J. Lee, H. S. Oh, U. Lee, *Chem. Eng. J.* **2021**, *424*, 130265.
[242] C. M. Gabardo, C. P. O'Brien, J. P. Edwards, C. McCallum, Y. Xu, C.-T. Dinh, J. Li, E. H. Sargent, D. Sinton, *Joule* **2019**, *3*(11), 2777–2791.
[243] W. Choi, S. Park, W. Jung, D. H. Won, J. Na, Y. J. Hwang, *ACS Energy Lett.* **2022**, *7*(3), 939–945.
[244] Y. Chae, K. Kim, H. Yun, D. Kim, W. Jung, Y. J. Hwang, U. Lee, D. K. LEE, B. K. Min, W. Choi, et al., *J. Mater. Chem. A* **2023**, *11*, 7025–7033.
[245] D. Corral, J. T. Feaster, S. Sobhani, J. R. Deotte, D. U. Lee, A. A. Wong, J. Hamilton, V. A. Beck, A. Sarkar, C. Hahn, et al., *Energy Environ. Sci.* **2021**, *14*(5), 3064–3074.
[246] D. L. T. Nguyen, C. W. Lee, J. Na, M. C. Kim, N. D. K. Tu, S. Y. Lee, Y. J. Sa, D. H. Won, H. S. Oh, H. Kim, et al., *ACS Catal.* **2020**, *10*(5), 3222–3231.
[247] D. Kim, W. Choi, H. W. Lee, S. Y. Lee, Y. Choi, D. K. Lee, W. Kim, J. Na, U. Lee, Y. J. Hwang, et al., *ACS Energy Lett.* **2021**, *6*(10), 3488–3495.
[248] Y. Lin, T. Wang, L. Zhang, G. Zhang, L. Li, Q. Chang, Z. Pang, H. Gao, K. Huang, P. Zhang, et al., *Nat. Commun.* **2023**, *14*(1), 3575.

[249] B. Yang, K. Liu, H. J. W. Li, C. Liu, J. Fu, H. Li, J. E. Huang, P. Ou, T. Alkayyali, C. Cai, et al., *J. Am. Chem. Soc.* **2022**, *144*(7), 3039–3049.
[250] M. Sithamparam, L. S. Lai, W. H. Tay, *Mater. Today Proc.* **2020**, *46*, 1922–1928.
[251] M. Jun, C. Kwak, S. Y. Lee, J. Joo, J. M. Kim, D. J. Im, M. K. Cho, H. Baik, Y. J. Hwang, H. Kim, et al., *Small Methods* **2022**, *6*(5), 2200074.
[252] S. Ringe, E. L. Clark, J. Resasco, A. Walton, B. Seger, A. T. Bell, K. Chan, *Energy Environ. Sci.* **2019**, *12*(10), 3001–3014.
[253] T. Cheng, Y. Huang, H. Xiao, W. A. I. I. I. Goddard, *J. Phys. Chem. Lett.* **2017**, *8*(14), 3317–3320.
[254] T. Liang, Y. T. Cheng, X. Nie, W. Luo, A. Asthagiri, M. J. Janik, E. Andrews, J. Flake, S. B. Sinnott, *Catal. Commun.* **2014**, *52*, 84–87.
[255] A. H. M. da Silva, S. J. Raaijman, C. S. Santana, J. M. Assaf, J. F. Gomes, M. T. M. Koper, *J. Electroanal. Chem.* **2021**, *880*, 114750.
[256] S. Liang, N. Altaf, L. Huang, Y. Gao, Q. Wang, *J. CO2 Util.* **2020**, *35*, 90–105.
[257] D. M. Weekes, D. A. Salvatore, A. Reyes, A. Huang, C. P. Berlinguette, *Acc. Chem. Res.* **2018**, *51*(4), 910–918.
[258] H. Yang, J. J. Kaczur, S. D. Sajjad, R. I. Masel, *J. CO2 Util.* **2020**, *42*, 101349.
[259] H. Xiang, S. Rasul, B. Hou, J. Portoles, P. Cumpson, E. H. Yu, *ACS Appl. Mater. Interfaces* **2020**, *12*(1), 601–608.
[260] A. Zahid, A. Shah, I. Shah, *Nanomaterials (Basel)* **2022**, *12* (8), 1380.
[261] L. Xue, C. Zhang, J. Wu, Q.-Y. Fan, Y. Liu, Y. Wu, J. Li, H. Zhang, F. Liu, S. Zeng, *Appl. Catal. B* **2022**, *304*, 120951.
[262] L. C. Pardo Pérez, A. Arndt, S. Stojkovikj, I. Y. Ahmet, J. T. Arens, F. Dattila, R. Wendt, A. Guilherme Buzanich, M. Radtke, V. Davies, et al., *Adv. Energy Mater.* **2022**, *12*(5), 2103328.
[263] S. Jiang, L. D'Amario, H. Dau, *ChemSusChem* **2022**, *15*(8), e202102506.
[264] G. A. Cerrón-Calle, T. P. Senftle, S. Garcia-Segura, *Curr. Opin. Electrochem.* **2022**, *35*, 101062.
[265] N. Zhang, B. Yang, K. Liu, H. Li, G. Chen, X. Qiu, W. Li, J. Hu, J. Fu, Y. Jiang, et al., *Small Methods* **2021**, *5*(11), 2100987.
[266] Z. Sun, H. Yin, K. Liu, S. Cheng, G. K. Li, S. Kawi, H. Zhao, G. Jia, Z. Yin, *SmartMat* **2022**, *3*(1), 68–83.
[267] E. Hu, C. Liu, W. Zhang, Q. Yan, *J. Phys. Chem. C* **2023**, *127*(2), 882–893.
[268] Z. W. Ulissi, M. T. Tang, J. Xiao, X. Liu, D. A. Torelli, M. Karamad, K. Cummins, C. Hahn, N. S. Lewis, T. F. Jaramillo, et al., *ACS Catal.* **2017**, *7*(10), 6600–6608.
[269] S. P. Liu, M. Zhao, W. Gao, Q. Jiang, *ChemSusChem* **2017**, *10*(2), 387–393.
[270] X. Ma, Z. Li, L. E. K. Achenie, H. Xin, *J. Phys. Chem. Lett.* **2015**, *6*(18), 3528–3533.
[271] Z. Li, X. Ma, H. Xin, *Catal. Today* **2017**, *280*, 232–238.
[272] J. Zhang, D. Chen, Y. Xia, Y.-P. Huang, X. Lin, X. Han, N. Ni, Z. Wang, F. Yu, L. Yang, et al., *J. Chem. Theory Comput.* **2023**, *19*(14), 4338–4350.
[273] N. E. Jackson, B. M. Savoie, A. Statt, M. A. Webb, *J. Chem. Theory Comput.* **2023**, *19*(14), 4335–4337.
[274] J. Wu, J. H. Li, Y. X. Yu, *Catal. Sci. Technol.* **2021**, *11*(4), 1419–1429.
[275] J. Wu, Y.-X. Yu, *Catal. Sci. Technol.* **2021**, *11*(21), 7160–7170.
[276] J. Wu, Y. X. Yu, *J. Colloid Interface Sci.* **2022**, *623*, 432–444.

Manuscript received: April 29, 2024
Revised manuscript received: July 10, 2024
Accepted manuscript online: July 18, 2024
Version of record online: September 6, 2024